Seismic and Hydroacoustic Observations of the 2016-17 Bogoslof Eruption

Authors: Gabrielle Tepp1, Robert P. Dziak2, Matthew M. Haney1, John J. Lyons1, Cheryl Searcy1, Haru Matsumoto3, and Joseph Haxel3

1. Alaska Volcano Observatory, U.S. Geological Survey, Anchorage, AK
2. NOAA/Pacific Marine Environmental Laboratory, Newport, OR
3. CIMRS, Oregon State University/NOAA, Newport, OR

Corresponding Author:

Gabrielle Tepp
4230 University Dr. Suite 100
Anchorage, AK 99508
907-786-7118
gtepp@usgs.gov

Keywords: volcano seismology, hydroacoustics, explosion seismicity, earthquake swarms, volcanic tremor

Acknowledgments

We would like to thank the FWS Tiglax crew for help in deploying the hydrophone and Geoff Lebon from NOAA-PMEL and the crew of the NOAA ship R/V Oscar Dyson for the recovery. AVO staff and others provided access to their data and analyses and helpful discussions throughout the eruption, for which we are grateful. Dane Ketner provided information about the seismic data return. Andy Lau was very helpful with the hydrophone data. Brian Shiro, Robin Matoza, and Alex Iezzi provided helpful comments on the manuscript. Seismic data (network code AV) is available through the IRIS Data Management Center. Hydrophone data is available from the NOAA Pacific Marine Environment Lab upon request to the authors. This paper is NOAA-PMEL contribution number 4954. Some figures were made with the GISMO Toolbox for MATLAB (Thompson and Reyes, 2018). GT was supported by the U.S. Geological Survey Mendenhall Fellowship Program. Any use of trade, firm, or product names is for descriptive purposes only and does not imply endorsement by the U.S. Government.

Abstract

In mid-December 2016, Bogoslof volcano, Alaska, began an 8.5-month-long eruption. Bogoslof is an emergent submarine volcano with only the very top forming a small island. Thus, the eruptive activity mostly occurred from a vent submerged beneath a bay or lagoon. The Bogoslof eruption was recorded on regional seismic and infrasound arrays as well as by a hydrophone that was deployed locally during the second half of the eruption. Since few emergent volcanic eruptions have seismo-acoustic recordings, these observations provide an opportunity to greatly improve our understanding of the seismo-acoustic signals produced by these eruptions. Here, we summarize the seismic and hydroacoustic observations of the eruption and put them into context with satellite and other observations of the eruption. The instruments detected a range of activity including earthquake swarms and explosive eruptions. Earthquakes occurred before, during, and after explosions as well as unassociated with explosions and as part of swarms. The seismic swarms can be further broken into 4 types: precursory, post-eruptive, general, and tremor-dominated. We examine the explosion seismicity in more detail, calculating an explosion tremor magnitude and analyzing the frequency content. The tremor magnitudes determined from the hydrophone data show a roughly linear relation to explosion plume height. Lastly, we categorize the activity into five eruption phases with differing character - precursory, opening, explosive I, pause, and explosive II - to outline the seismic and hydroacoustic story of the eruption.

Introduction

After 24 years of quiet, Bogoslof volcano unexpectedly began erupting in December 2016. The 8.5-month-long eruption was defined by at least 70 major explosive eruptions (herein 'explosions'), some of which sent ash plumes up to 12 km above sea level (Coombs et al. 2019). Typical for historical Bogoslof eruptions, lava domes were also produced: a cryptodome which emerged early in the eruption and two later lava domes that were destroyed by explosions within days of forming (Waythomas & Cameron 2018; Coombs et al. 2019). The main period of eruption can be broken into two explosive phases with a 9-week pause in between.

Bogoslof is located north of the main arc of the central Aleutian Islands of Alaska (Figure 1). While primarily a seamount, the summit of Bogoslof reaches above sea level, forming the small Bogoslof Island. Over the course of the eruption, Bogoslof Island changed dramatically in morphology and size (Waythomas et al. 2019). Most explosions during the 2016-17 eruption occurred in a partially or fully submerged vent located in a bay or lagoon, depending on the morphology of the island at the time of the explosion. However, there is evidence for eruptive vents drying out during some explosions (Fee et al. 2019). The volcano is also unmonitored, with near-real-time observations of the eruption provided primarily by regional (>50 km) seismic and infrasound (Lyons et al. 2019) networks, satellites (Lopez et al.

2019; Schneider et al. 2019; Waythomas et al. 2019), and regional lightning sensors (Van Eaton et al. 2019). Because Bogoslof is predominantly a seamount, coupling of seismic energy into the water column produced detectable hydroacoustic phases. Thus, a local campaign hydrophone was deployed during the second half of the eruption to provide more detailed recordings.

For a near or at sea-surface ("emergent") eruption, the Bogoslof eruption was well-recorded seismo-acoustically despite being primarily recorded by regional instruments. Only 10 such eruptions occurring at 7 seamounts and on one submarine volcanic flank, including Bogoslof in 2016-17, have confirmed reports of seismic, hydroacoustic, or acoustic recordings for at least part of the eruption (Table 1). Eight of those have seismic observations, while 6 have hydroacoustic observations and only 4 have acoustic observations. The Bogoslof eruption is the first emergent eruption to have all three types of seismo-acoustic observations with modern instrumentation. However, the 2010 submarine eruption of South Sarigan seamount (~180 m below sea level) in the Mariana Islands was recorded by all three observations types as well (Green et al. 2013; Searcy 2013). The only other emergent eruption with all observation types was the 1958 eruption of Capelinhos, on the flank of Fayal volcano in the Azores, which had minimal acoustic and hydroacoustic recordings and was only recorded on one seismograph (Machado et al. 1962; Richards, 1963). The Bogoslof eruption also had the longest duration of seismo-acoustic observations, with seismic and infrasound data available throughout the entire eruption.

The 2016-17 Bogoslof eruption produced a variety of seismic activity. Much of this seismicity played a key role in detecting the explosions and occasional precursory activity, allowing for timely responses and hazard notifications (Coombs et al. 2018). Here, we first describe and examine the seismicity and hydroacoustic activity observed during the eruption: earthquakes, seismic swarms, explosion-related seismicity, and other activity. We then combine our observations to outline the seismic chronology of the eruption within the context of other geophysical, geological, and satellite observations of the eruption.

Data

Bogoslof is an unmonitored volcano with no local instrumentation. Therefore, the Alaska Volcano Observatory (AVO) monitored the eruption seismo-acoustically using nearby seismic networks on Umnak (>45 km away) and Unalaska (>70 km away) islands (Figure 1) as well as several regional infrasound arrays (Lyons et al. 2019). The seismic networks have a mix of short-period (100 samples per sec) and broad-band (50 samples per sec) instruments. Periodic and extended outages of the stations (Table 2) further hampered detection capabilities of the already limited regional data. Given the remote location of the region, weather-related noise levels were also sometimes high enough to mask eruption-related signals, especially during the winter months. All times are given in UTC, and all figures of seismic data in this paper show the vertical component of the seismometer.

A single hydrophone mooring was deployed ~7 km northeast of Bogoslof on 22 May 2017 and recorded continuously at 2000 samples per second until being retrieved on 2 October 2017 (Figure 1). The data was not telemetered and was therefore not used for real-time monitoring. The mooring consisted of a float, hydrophone instrument package, acoustic release, and an anchor (Figure 2a; Haxel et al. 2013). The mooring was deployed on the northeastern flank of Bogoslof at a water depth of ~1500 m with the instrument situated at 231 m depth.

Hydroacoustic Propagation

Much of the seismicity from the eruption produced seismic waves that were able to convert into hydroacoustic waves at the seafloor. Seismicity occurring within the seamount was particularly well-suited to conversion (Wech et al. 2018). Hydroacoustic phases were recorded by the hydrophone and sometimes on the seismometers. When detected seismically, two conversions are present – the first from seismic to hydroacoustic and the second from hydroacoustic back to seismic. For hydrophone detections, only the first conversion is present unless the activity is at or near enough to the seafloor to directly produce a hydroacoustic wave. In this study, we refer to all phases propagating primarily through the water as T-phases, whether they were detected by the seismometers or the hydrophone. On the Umnak and Unalaska seismic networks, T-phases typically arrived 20-30 sec after the P-phase due to the much slower propagation speed in water and were not recorded on all stations.

The hydroacoustic sound speed profile in the region is a polar half-channel (e.g., Kutschale 1969) with a near-surface (<~400 m depth) low-velocity layer in the summer months, the time of year the hydrophone was deployed. Sound speed profiles approximated from Profiling Float (PFL) data gathered during the summer of 2007 as part of the US ARGO Project show that the surficial channel is thicker but less pronounced toward the east of Bogoslof, where the hydrophone is located, compared to the west (Figure 2b&c). The hydrophone instrument was situated near the axis of the channel to improve its detection capability.

T-phases from volcanic activity have been detected by seismometers and hydrophones after traveling long distances through the ocean, in a few cases greater than 14,000 km (e.g., Dziak & Fox 2002; Metz et al. 2016; Tepp et al. 2019), due to the low attenuation of water and channeling of the energy in the deep-ocean low-velocity sound channel (e.g., Dietz & Sheehy 1954; Talandier 2004; Green et al. 2013)al.al.. However, as previously discussed, the higher latitude Bering Sea has only a small low-velocity channel very near the surface, usually only in the summer months (Figure 2b). Typically, the sound velocity increases approximately linearly with depth in polar regions, requiring more sea-surface reflections and associated energy loss. Despite this, several Bogoslof eruptions were detected by the seismic network on Tanaga Island, ~700 km away in the western Aleutians (Figures 1 & 3). The station TANO, on the northwestern shore of Tanaga, seemed particularly well-suited to detecting reflections off of the submarine Bower's Ridge (Figure 1 inset), adding an extra ~120 km to the distance traveled. The best distant T-phase detections occurred on 8 March 2017 (event 37) and 30 June 2017 (event 55). We also looked for signals from the Bogoslof eruption on the International Monitoring System hydrophone arrays at Wake Island. Unfortunately, no detections were found likely because the path from Bogoslof to these arrays is blocked by topography (e.g., Unalaska and Umnak Islands).

Earthquakes

Earthquakes were a common occurrence throughout the Bogoslof eruption. Most earthquakes, however, were too small to be located from recordings on the distant seismometers. AVO analysts located 244 earthquakes between 22 December 2016 and 8 August 2017 with magnitudes between 0.6 and 2.8. The Alaska Earthquake Center (AEC) located an additional 18 earthquakes near Bogoslof between 28 September 2016 and 30 June 2017 with magnitudes between 1.4 and 2.2. Following the method described by Thompson & West (2010), we calculate an equivalent local magnitude for the entire catalog (AVO+AEC) of 3.26. This value is about the same as that for the earthquake catalog of the 2009 Redoubt eruption. Given the distance to the closest seismic stations and their poor azimuthal coverage, the hypocenters have large errors and are poorly constrained (Supplementary Material S1).

The located earthquakes were categorized as swarm, precursory, co-eruptive, or sporadic. Swarm earthquakes were defined as those that occurred in groups of at least 5 within 3 hours. In the next section ("Seismic Swarms"), earthquake swarms are further categorized based on their relation to the explosions. Earthquakes that preceded explosions, typically by no more than a few minutes, but were not part of a swarm were considered precursory. Co-eruptive earthquakes were those that occurred during explosive eruptions (see "Characteristics of Explosion Seismicity" section). Lastly, sporadic referred to the remainder – individually occurring (i.e., non-swarm) earthquakes without any clear relation to the explosions. About 87% (228) of the AVO+AEC catalog earthquakes occurred during a swarm, with most coming from three periods (19-20 February, 10-13 March, and 15-16 April). Only 3 precursory earthquakes were locatable along with 15 sporadic and 16 co-eruptive earthquakes.

A variety of seismic phases were recorded for the Bogoslof earthquakes which may be linked to their locations, depths, and/or source processes (Figure 4a&b). On a few stations, notably MAPS and OKFG, a secondary P-phase was commonly observed and was useful for identifying earthquakes as coming from Bogoslof. This secondary P-phase is likely a reflection off the Moho, given that it only appears for some earthquakes when the propagation path to those stations is right for reflection near the critical angle. The S-phase amplitudes varied quite widely. In particular, co-eruptive and non-swarm precursory earthquakes often had weak S-phases compared to the P-phase amplitudes. This may be due to shallow hypocenters, source processes, or both. Many of the earthquakes also had associated T-phases, as described in the "Hydroacoustic Propagation" section.

The hydrophone recordings of the earthquakes also appear to have at least two phase arrivals (Figure 4c). The second arrival (T2) is the expected T-phase, converted near the source, and typically has a much larger amplitude. The first, weaker phase (T1) is most clear in waveforms of stronger earthquakes or stacks of weaker earthquakes and tends to have less high frequency energy. This phase is likely a P-phase that converts to a T-phase somewhere near the hydrophone mooring. The arrival time difference between the two phases is typically around 0.8-1.5 sec, which is similar to the expected time difference for a P-phase converted at the mooring base and a T-phase converted near the source. However, P-phases can also be directly detected by seismic shaking causing depth changes of the mooring that are large enough to be recorded, and this explanation for the first arrival (T1) cannot be completely ruled out.

Many of the earthquakes produced during the eruption were too small to be located with the regional seismometers, often being detected by only 1 or 2 of them, and therefore were not included in the AVO catalog. To better estimate and characterize the earthquake activity, Wech et al. (2018) created a matched-filter earthquake catalog. Starting with the AVO and AEC catalog, they identified repeating earthquake families and performed a single-station matched-filter analysis (minimum cross-correlation value of 0.4) from September 2016 through September 2017 using 3-component data from MAPS, which was operational for most of the eruption (Figure 1 & Table 2). This approach generated a catalog of 3199 earthquakes (estimated M_L ranging from 0.5-2.5), which is 12 times as many as the AVO and AEC catalog.

A matched-filter earthquake catalog was also produced for the hydroacoustic data. We applied a matched-filter detector using templates generated by the RESA detector (Tepp 2018) and supplemented with hand-picked earthquakes to data recorded between 23 May and 1 September 2017. RESA templates and hand-picked earthquakes were combined if they correlated at the minimum value of 0.7, resulting in 43 templates. The data were filtered from 8-20 Hz to avoid false detections from frequent noise below ~8 Hz. The resulting catalog included 5292 events. This is much more than the seismic matched filter catalog found for the entire eruption, demonstrating the greater sensitivity of the local hydrophone compared to the regional seismic stations.

Seismic Swarms

Analyzing seismic swarms can provide insight into periods of elevated seismicity during eruptions, typically indicating subsurface magma movement or other stress changes in the volcanic system (e.g., White et al. 1998; McNutt 2005). A total of 47 seismic swarms were manually identified in seismic data recorded between September 2016 and the end of the eruption on 30 August 2017 (Supplementary Material S2). The swarms were categorized as precursory, post-eruptive, general, or tremor depending on their temporal relation to the explosions and whether they were dominated by earthquakes or tremor (e.g., Figure 5). Precursory swarms were those that ended within 4.5 hours before an explosion onset. Post-eruptive swarms were those that started within 4.5 hours after the end of an explosion. General swarms did not have any clear relation to the explosions, and tremor swarms primarily comprised tremor bursts rather than earthquakes. Table 3 lists the 26 major seismic swarms, defined as those with at least 20 earthquakes except for the tremor swarm. The major swarms were labeled with a letter indicating the swarm type (P=precursory, A=post-eruptive, S=general, and T=tremor) and a number giving the chronological order of the swarm, with each type numbered separately. Of the major swarms, 15 were precursory to explosions and 2 were classified as post-eruptive. Eight were general swarms not directly associated with a known explosion. Only 1 was a tremor swarm dominated by short tremor bursts rather than earthquakes.

The earthquake counts in each swarm were determined with the seismic matched filter catalog since it is more comprehensive than the AVO catalog. A swarm onset was chosen when the earthquake rate reached a minimum of 5 earthquakes in 3 hours, with the swarm ending when the rate dropped below this. Some manual division was necessary to separate the types of swarms and earthquakes (e.g., precursory and co-eruptive) that might otherwise blend together simply based on earthquake rates. Only earthquakes with a cross-correlation value of 0.405 or above were included. Three of the major swarms (P3, A2, & P5) occurred during outages of station MAPS and, thus, do not have any associated earthquakes in the matched filter catalog. The average earthquake rate was determined by dividing the number of earthquakes by the swarm duration. The maximum rate was determined as the maximum number of earthquakes in a 15 min window using windows that overlapped by 10 min throughout the swarm duration. Figure 6 shows rates, earthquake counts, and durations for all swarms with values provided in Table 3 and Supplementary Material S2. Most swarms were less than 10 hours long (83%), had fewer than 50 earthquakes (78%), and had average earthquake rates below 20/hr (88%).

Twenty-five earthquake swarms were observed to have increasing rates that reached a high enough rate that the waveforms overlapped and appeared as tremor, with 19 of these leading into an explosion (Figure 5a, Table 3, & Supplementary Material S2). These swarms were useful for short-term forecasting of explosions (Coombs et al. 2018; Tepp 2018). Similar accelerating swarms have previously been observed at other volcanoes before explosions (e.g., Ketner & Power 2013; Tameguri & Iguchi 2019) and dome collapses (e.g., Neuberg et al. 2000; Powell & Neuberg 2003). However, during 11-16 December (including swarms S2, P1, A1, P2, and 4 unnumbered swarms), there was nearly continuous seismicity in which earthquakes merged into tremor and tremor separated into earthquakes (Figure 5e). Evidence from infrasound and satellite data suggest that an explosion (event 4) occurred at the end of that period with other surficial activity occurring throughout it (Coombs et al. 2019; Lyons et al. 2019; Schneider et al. 2019). All of the seismically-recorded swarms that were observed to merge into tremor occurred during the first half of the eruption.

The precursory swarm on 31 May 2017 (P15) was different than the other precursory swarms. It peaked and ended ~4.5 hours before the explosion onset, with only minor, occasional tremor or sporadic earthquakes in between, and never reached a high enough rate for the earthquakes to merge into tremor. In some ways, this swarm was more similar to the general swarms, which may indicate that the source process producing it was different than that of the other precursory swarms. Similar swarms occurring a few hours before explosions have been reported at Sakurajima volcano, Japan (Nishi 1974 via Tameguri & Iguchi 2019). See Tepp & Haney (2019) for further analysis and discussion of the precursory swarms.

Only 7 post-eruptive swarms were identified using the minimum 5 earthquake threshold. All but two of the post-eruptive swarms had fewer than 20 earthquakes (Figure 6e&f; Supplementary Material S2). The swarms also had relatively low earthquake rates with none exceeding an average rate of 8/hour and only one (A1) with a maximum rate above 12/hour (Figure 6b-d; Figure 5b; Supplementary Material S2). The two major post-eruptive swarms (A1 & A2) occurred in mid-December during the period when earthquakes merging into and out of tremor were frequent and were classified as post-eruptive due to their occurrence soon after explosions. These swarms stand out from the other post-eruptive swarms and have characteristics (e.g., rate changes) that are more similar to the precursory swarms, particularly those in mid-December (compare Figure 5a,b,&e). The A2 swarm even increased in rate, briefly merging into tremor at the end, and could be a precursory swarm to a small, unidentified explosion. The earthquakes in the unnumbered post-eruptive swarms also differed in character from those in the A1 & A2 swarms with more sharply defined P-phase onsets and weaker T-phases (e.g., Figure 4). The earthquakes in the unnumbered post-eruptive swarms were likely deeper, brittle-failure type events caused by stress adjustments in the volcanic system.

There were 17 general earthquake swarms observed with no clear relation to any major explosion (Figure 5c; Supplementary Material S2). Of these, 8 were considered major swarms (Table 3). The character of most of these general swarms differed from that of the precursory or post-eruptive swarms, though 3 unnumbered swarms in December 2016 were similar in character to precursory swarms (e.g., merged into tremor) and may have been associated with small, unidentified explosions. While the general swarms had variable earthquake rates that were comparable to the precursory swarms (Figure 7b&d), the rates typically did not get high enough to result in significantly overlapping waveforms (i.e., they did not merge into tremor) except for those previously noted. The lack of tremor may be due in part to the general swarms typically having earthquakes with weak T-phases (e.g., Figure 4) and, thus, shorter duration waveforms which would require a higher rate to be observed as tremor. The most notable general swarms occurred in late September 2016 (S1), mid-April 2017 (S7), and mid-August 2017 (S8). These three swarms in particular were likely produced by magma intrusions, based on when they occurred in relation to other seismic and surficial activity and on the swarm characteristics (e.g., earthquake rate changes). However, other smaller swarms may also be linked to intrusions. Two swarms (S5 & S6) categorized as general swarms occurred in mid-March 2017 before a precursory swarm (P14). While the three swarms had only short pauses between them and by some measures might be considered a single swarm, there was some difference in the earthquake character of each, especially in the first swarm (S5). This suggests that there was a change in source location or process for each of these swarms.

Hydrophone-detected Swarms

There were 33 earthquake swarms identified in the hydrophone data, most of them initially through the use of the hydroacoustic matched filter catalog (Supplementary Material S3). However, earthquakes in 15 swarms did not match any of the templates and were manually identified. Sixteen of the swarms ended within a few hours of an explosion and are considered precursory, and 3 swarms were post-eruptive. Following the same parameters as for the seismically-determined swarms, 17 of the swarms could be considered major swarms with at least 20 earthquakes (Table 4). The major swarms were labeled similarly to the major seismic swarms but include an "H" to indicate that they were hydroacoustically determined. Earthquake counts and rates and swarm durations are plotted in Figure 7 for 18 swarms recorded in the hydroacoustic matched filter catalog. Similar to the seismically-derived swarms, the post-eruptive swarms tended to have lower earthquake rates (Figure 7b&d) and fewer earthquakes (Figure 7f).
Seven swarms with a similar character occurred during 22-24 August 2017, six of which were undetected by the matched filter detector. The one that was detected had most of its earthquakes matching the hand-picked templates, which were chosen from that swarm. These swarms, therefore, do not appear to comprise repeating earthquakes. In addition to earthquakes, these swarms also contained bursts, about 1 minute long and typically comprising multiple impulses, that could be small explosions, including one on 22 August that had an infrasound signal (event 65). The bursts were also similar to the tremor bursts in the T1 seismic swarm (during the HP7a swarm; Figure 5d) although with lower amplitudes.

At least part of three swarms (end of HP5, HP7b, & unnumbered swarm on 6 June 2017) had very high event rates, rarely falling below ~10 events/min. Such swarms were only observed on the hydrophone. When observed in the seismic recordings, these rapid rate events (RREs) appeared as tremor, likely from overlapping waveforms. The RREs are thought to be a more extreme version of the precursory swarms that increase in rate leading up to explosions (Tepp and Haney 2019). The HP7b RRE swarm increased to a high and consistent enough earthquake rate that it merged into a gliding harmonic tremor (Tepp and Haney 2019), similar to an observation during the 2009 eruption of Redoubt volcano, Alaska (Hotovec et al. 2013).

Six earthquake swarms were recorded by both the hydrophone and seismic stations: two major earthquake swarms (P15/HP1 and S9/HS4), unnumbered post-eruptive swarms on 13 June, 29 May, and 7 August 2017, and the tremor swarm (T1/part of HP7a). In the case of P15, S9, and the 29 May swarm, the hydrophone was able to detect more earthquakes than the seismic stations. Many of these extra earthquakes occurred near the beginning of the swarms when the earthquake amplitudes were smaller. Because the hydrophone detected more of the early earthquakes, the duration of the swarms was longer on the hydrophone as well. In the case of the 29 May swarm, the extra detections on the hydrophone allowed it to be classified as a post-eruptive swarm, whereas the seismometers did not start to detect the earthquakes until about 5 hours later. During the S9 swarm, low-frequency noise in the hydrophone data strongly increased around the time that the seismic stations began detecting S9 earthquakes, ~4 hours after the hydrophone began recording earthquakes. Shortly after the hydrophone noise decreased, seismic noise began to increase. Thus, it is difficult to directly compare the detections of this swarm in the seismic and hydroacoustic data. However, when earthquakes were recorded in both data types they tended to have similar rates, suggesting that the seismometers were recording most of the activity. Most of the earthquakes in the 13 June and 7 August post-eruptive swarms were strong enough, or perhaps occurred in a good location for conversion and propagation, to be detected on both the seismometers and the hydrophone. This suggests that for at least some swarms, the seismic recordings are not missing much additional activity despite the lower detection capability of the regional instruments. The tremor swarm occurred during a long earthquake swarm detected by the hydrophone and is otherwise very similar in both data types. The tremor swarm is possibly a pulsatory explosive eruption; however, there were no infrasound detections during the swarm.

Characteristics of Explosion Seismicity

Between 12 December 2016 and 30 August 2017, Coombs et al. (2019) identified 70 major explosions, with a few smaller ones later identified and left unnumbered. However, the exact number of explosions is somewhat open to interpretation as several of the numbered explosions had multiple sub-events occurring up to an hour apart. Searcy and Power (2019) examined the pulsatory nature of explosions and identified 118 events that they deemed “eruptive episodes” based on the duration of high amplitude seismic signals. Their eruptive episodes often contained multiple pulses separated by lower amplitude tremor. Several tremor bursts possibly associated with small explosions were also identified in the hydroacoustic data but could not be identified or were only very weakly visible in the regional seismic or infrasonic data. Here, we present basic analyses of the 70 numbered explosions.

Various seismicity accompanied the explosions, primarily in the form of seismic tremor and co-eruptive earthquakes. Additionally, Haney et al. (2019a) analyzed the wavefield composition of the eruption tremor and estimated reduced displacement, a standard measure of tremor intensity, for some of the explosions.

For each of the 70 explosions, we determined a maximum amplitude and tremor magnitude for both the seismic and hydroacoustic recordings to examine how the size of the explosions progressed throughout the eruption (Figure 8b&c). The maximum amplitude was measured as the maximum value of the absolute value of the waveform. The tremor magnitude, TM, was defined as:

$$TM = log10(\Sigma|amplitude|)$$

with the sum taken over the duration of the explosion, here defined simply as the end time of the last signal minus the start time of the first signal with no regard to pauses in between pulses (Figure 8a). The TM was chosen as a way to calculate an explosion "size" while accounting for the clipping that occurred on the hydrophone recordings. Of the 30 numbered explosions recorded by the hydrophone, 12 had no clipping, 11 had only minor clipping with little data affected, and 7 had moderate to severe clipping (see Supplementary Material S4). Instrument responses were removed before the TM calculation. Seismic data were band-pass filtered from 1-20 Hz and hydrophone data from 5-75 Hz. The lower end of the hydrophone filter was chosen to help exclude frequent strong, low-frequency signals that are likely related to strumming of the mooring line.

There were no systematic changes in the TM over the course of the eruption (Figure 8c). However, clusters of lower TM explosions occurred while the lava domes were present in the second half of the eruption. The lowest TM explosion in the first half of the eruption occurred on 22 December 2016 (event 8), one day after the first lava dome became visible (Waythomas et al. 2019). The TM calculated from station OKER is higher than that at MAPS which is a consequence of its more proximal location (53 km vs 73 km distance) and local site effects. The hydrophone has different units, so the TM values are not directly comparable to those from the seismic. However, the seismic and hydrophone TM follow a similar pattern over the course of the eruption and have a roughly linear relationship (Figure 8c&f). This suggests that the hydrophone is likely recording converted seismic phases rather than direct hydroacoustic phases.

We also compared the TM to the estimated plume heights (Schneider et al. 2019). There is no clear relation between the seismic TM and the plume heights, but there does seem to be a roughly linear relationship between the hydroacoustic TM and the plume heights (Figure 8g). Given that the hydroacoustic data were only recorded during the second half of the eruption, this relation could be applicable to only the later part of the eruption. Examining the seismic TM for the first and second halves of the eruption separately shows no clear relationship for the first half and a marginal relation for the second half (Supplementary Material S5), supporting the conclusion that the relation may only be applicable to the second half. Other possible explanations for why the TM-plume height relation is most apparent in the hydroacoustic TM are that the relation is only valid for the hydroacoustic recordings or that uncertainty in the seismic TM measurements from noise and propagation effects is large enough to hide any potential relation. In contrast, Haney et al. (2019a) found a weak relation between seismic reduced displacement (a standardized tremor amplitude measurement) and plume heights of some explosions in the first half of the eruption. Thus, it is possible that different seismic parameters were better related to plume heights at different times during the eruption.

The maximum amplitudes, plotted as log amplitude, show a similar pattern to the tremor magnitudes (Figure 8b&c); however, the clipping on the hydrophone becomes apparent. Because maximum amplitudes are more prone to fluctuations in the recorded waveform due to noise and other spurious signals, the maximum amplitudes are also more variable than the tremor magnitudes. The 24 June (event 52) and 13 June 2017 (event 49) explosions had the highest maximum amplitudes on MAPS; however, these were both very pulsatory explosions, so the maximum amplitudes may have been from intervening earthquakes or noise rather than the explosion seismicity. Neither of those explosions has a particularly high tremor magnitude. Similarly, the highest maximum amplitude explosion on OKER was on 23 December 2016 (event 9), though that explosion does not have a particularly high tremor magnitude.

We also calculated the frequency index and the average frequency of the co-eruptive tremor (Figure 8d&e). The frequency index is calculated as $FI = log(\frac{Ahigh}{Alow})$ where A_{high} and A_{low} are the average amplitudes of the signal in high and low frequency bands (Buurman and West 2010). The frequency bands used were 1-3 Hz and 3-15 Hz for the seismic data and 5-20 Hz and 20-50 Hz for the hydrophone data. The average frequency was calculated by normalizing the inner product of the power spectral density and the frequency vectors in the spectral domain. Instrument responses were removed before these calculations, and the average frequency was calculated on data that had used the filters described in the TM paragraph above.

The seismic recordings of the eruptions have little variation in frequency content. Most of the seismic energy was below ~5 Hz, with few explosions having higher frequency content. This is likely a result of attenuation acting over the regional distances from the volcano to the sensors. Some of the explosions on OKER have higher frequencies which are likely from ground-coupled airwaves recorded on that station. The hydrophone frequency content shows more variation, with larger explosions typically having more high frequency content. However, the clipping, especially of the largest events, has likely affected these results. The hydrophone recordings also often have strong energy bands in the 2.5-8 Hz range that are likely from strumming of the mooring cables and may also affect the frequency analysis. For comparison, Lyons et al. (2019) found that the explosion infrasound had a higher low-to-high frequency content ratio than is typical for subaerial eruptions.

Thus, the strong low frequencies in the seismic data may be in part a reflection of the source rather than simply attenuation along the propagation path.

Earthquakes sometimes occurred during explosive eruptions along with the tremor. A few of these earthquakes even reached magnitude 2-2.5. Of the 70 numbered explosions, 23 had enough co-eruptive earthquakes to be considered a swarm (5 earthquakes in 3 hrs), with 12 of these swarms having 20 or more earthquakes (Table 5 & Supplementary Material S2 & S6). Swarm statistics were determined in the same way as previously described for the seismic swarms. The explosions on 8 March (event 37) and 7 August (event 63) had by far the most co-eruptive earthquakes; however, these two explosions were among the longest in duration, so the average earthquake rates were similar to those of other explosions with major swarms. Co-eruptive earthquake swarms became more common as the first half of the eruption progressed, with few accompanying December explosions; however, only 25% of the explosions in the second half of the eruption had co-eruptive swarms compared to 42% in the first half (Supplementary Material S6a). The major co-eruptive swarms were evenly split with 6 occurring in each half (Table 5). Higher TM explosions were more likely to have co-eruptive swarms (Supplementary Material S6b), suggesting that the larger explosions produced more earthquakes. The hydrophone recorded co-eruptive swarms during 7 of the explosions based on the matched-filter catalog; however, the templates used to produce the catalog did not intentionally include co-eruptive earthquakes, so many may have been missed.

Other Seismicity & Hydroacoustic Activity

In this section, we describe other types of seismicity or hydroacoustic activity beyond the earthquakes, seismic swarms, and explosions that were noted during the eruption. We also examined the data for any seismicity associated with non-explosive subaerial eruptive activity (e.g., extrusion of lava domes) to provide more insight into those processes. In addition to the activity described here, Haney et al. (2019b) documented hydroacoustic signals associated with volcanic lightning and interpreted them as being high frequency volcanic thunder acoustically transmitted from the atmosphere into the ocean.

Harmonic Tremor

Three instances of gliding harmonic or monochromatic tremor were seismically recorded prior to eruptions on 26 December 2016 (event 10), 4 January 2017 (event 15), and 30 June 2017 (event 55). Each of these glides evolved differently over time and had a duration of 5 min, 75 sec, and 2 min, respectively. The hydrophone recorded the 30 June glide as well as two more possible glides before explosions on 13 June 2017 (event 49b) and 5 July 2017 (event 58) that weren't detected by the seismometers. See Tepp and Haney (2019) for more information about the precursory glides.

In addition to the precursory glides, downward-gliding harmonic tremor was also observed on 2 July 2017, ~25 min after explosive event 56 in both seismic and hydroacoustic data (Figure 9). This glide was immediately preceded by an earthquake and followed by a tremor burst lasting ~2.5 min.al.al. The sequence of events is reminiscent of the explosion sequence on 30 June 2017 (event 55) and may be a weaker explosion. However, the timing between the seismic and hydroacoustic arrivals is different, though it's still plausible for a source at Bogoslof, especially one on or near the southwestern slope. There was also no observation of associated surficial activity. Another possible interpretation is an underwater landslide (c.f., Schöpa et al. 2018) or some other geological process. The glide itself could result from a stick-slip process with a decreasing rate of events (e.g., Hotovec et al. 2013) or increasing patch size (e.g., Schöpa et al. 2018), such as might be expected preceding a landslide.

Mass Flow Events

In the hydroacoustic data, explosions on 24 June (event 51), 27 June (event 54), 5 July (event 58), and 27 August 2017 (event 66) were followed by very broad-band signals that were several to tens of minutes long and started before the explosion tremor ended (Figure 10). The signals have a diffuse character with no strong dominant frequency band up to the ~500 Hz Nyquist frequency of the hydrophone. Some frequency banding is visible in the first 3 cases, especially near the end of the signals, and is likely a result of wave interference (e.g., Lloyd's mirror effect - Carey 2009). These signals were not recorded by seismic or infrasound sensors, suggesting that they likely occurred underwater, on or just below the seafloor. Somewhat similar diffuse signals were recorded by seismometers after explosions during the 2009 eruption of Redoubt, Alaska (Buurman et al. 2013). These signals were interpreted as mass flow events, primarily lahars but also pyroclastic flows. Drobiarz (2017) also analyzed similar diffuse signals recorded by hydrophones during an eruption of West Mata seamount, NE Lau Basin, in 2009-2010 and interpreted them as landslides. However, the diffuse nature of the signals is similar to that of sediment flow in streambeds recorded by hydrophones (J. Ball, pers. comm.), suggesting that they result from a looser, turbulent flow of material rather than a large ground movement as would be expected for landslides. Thus, the diffuse, post-eruptive signals observed during the Bogoslof eruption are likely mass flow events occurring on the submerged volcanic flank where a resulting hydroacoustic signal would be stronger than a seismic signal.

Lava Domes

There were no obvious seismic signals associated with the growth of the lava domes present from around 5-10 June and 18-27 August (Waythomas et al. 2019). However, event 43 (5 June 2017) appears to be a seismic-only event with no activity recorded by any of the other data types beyond a report and photos of steaming and a white plume up to a few thousand feet. The seismic-only signal on 5 June could be indicative of magma moving up from depth, with the plume resulting from hot magma interacting with cool water and/or simultaneous degassing. The first satellite image of the dome breaching the sea-surface was taken mid-day on June 5

(Coombs et al. 2019), suggesting that the dome was submerged prior to that. The S8 swarm began 3 days before the August dome was identified in satellite data. Earthquakes from this swarm were detected in the hydroacoustic data and occasionally in the seismic data through much of 17 Aug. Similar to event 43, the S8 swarm could have been associated with magma first moving toward the surface, eventually producing the dome within a few days. The first satellite confirmation of the dome came on 18 August (Coombs et al. 2019). From 19-24 August, the hydrophone recorded occasional short swarms of earthquakes, sometimes including small bursts of activity ~1 minute long that could be explosions (e.g., event 65), as described in the subsection "Hydrophone-detected Swarms". The bursts of activity were typically recorded as weak tremor in seismic data, but only event 65 on 22 August was detected by infrasound sensors. It is unclear if there is any relation between these swarms and the growth of the August lava dome.

One lava dome (cryptodome) was produced early in the eruption sequence and was not destroyed during the eruption. Satellite images show the first sign of this dome on 21 December 2016, but it may have begun growing sooner (Waythomas et al. 2019). It is possible that the swarm and tremor activity between 11-16 December was associated with the initial growth of this dome. Similar earthquake swarms have been noted during the extrusion of lava domes and plugs at other volcanoes (e.g., White et al. 1998; Iverson et al. 2006; Thelen et al. 2011). Loewen et al. (2019) determined that the December dome was composed of non-vesicular and crystalline rock with a different composition than the most common basaltic tephra and bombs known to be ejected during the eruption. They suggest that the dome was extruded as mostly solid rock, so related seismicity would not be unexpected. The June and August lava domes, however, are thought to have been composed of fresher, less solidified magmas similar to the trachybasaltic tephra and bombs, which may explain the lack of, or weaker, seismicity during the effusion of those domes.

Seismic Chronology

Figure 11 shows the overall seismic progression of the eruption in terms of the root-mean-square (RMS) amplitude of the continuous data and earthquake rates with the numbered explosion onsets and major seismic swarms marked. RMS amplitude can be strongly affected by noise, which was certainly true for the seismic RMS amplitude. Due to the distance of the seismometers from Bogoslof, the seismic signals often have relatively low signal-to-noise ratios. In comparison, the hydroacoustic RMS amplitude shows a better correlation with the explosions and earthquake activity. While the hydrophone was much closer to Bogoslof and could record higher amplitude signals from the eruptive activity, low frequency noise was common, resulting in RMS amplitude peaks unrelated to the explosions and seismic swarms.

Using the seismic observations described in previous sections and shown in Figure 11, we divide the 2016-2017 Bogoslof eruption into five phases of activity. These phases are largely the same as those proposed by Coombs et al. (2019), except that we include an additional phase in mid-December which was seismically unique.

27 September to 10 December 2016 – Precursory Phase:
The eruption had some precursory seismic activity that was primarily noticed in hindsight since Bogoslof is unmonitored and earthquakes originating there may be mistaken for regional seismicity. The first major precursor was an earthquake swarm lasting ~18 hours on 28 September (S1; Table 3), which was likely caused by an initial magma intrusion. A low-rate swarm of earthquakes occurred in early October, with sporadic earthquakes continuing until the next major eruption phase. Additionally, a few earthquakes were found with the matched-filter detector going back to at least mid-July 2016, although no comprehensive search was done.

11 December to 15 December 2016 – Opening Phase:
The Precursory Phase was followed by a period of near-continuous earthquakes and tremor. Earthquakes were observed increasing in rate before merging into tremor that was sustained for minutes to hours (e.g., swarms P1, A1, and P2). The tremor sometimes ended by dividing into individual earthquakes with a decreasing rate (e.g., A1; Figure 5e). The first occurrence of merged-earthquake tremor occurred on 12 December (P1) and was coincident with the first detection of infrasound (Lyons et al. 2019). Two numbered explosions occurred on 12 December (events 1&2); however, these appear to be different than the other explosions with higher frequency infrasound (Lyons et al. 2019). Fee et al. (2019) analyzed the frequency content of these events and determined that the vent was likely subaerial at the time. Additionally, neither produced a plume that was detectable in satellite data (Schneider et al. 2019). This type of seismicity was observed for nearly the full 4-day period, primarily on the station MAPS. Unfortunately, MAPS was offline for much of 13-14 December, with no clear activity observed on other stations. However, activity continued throughout the periods when MAPS was online, suggesting that it was persistent while the data was out. The seismicity in the Opening Phase is possibly related to the initial growth of the December lava dome. The first satellite confirmation of emissions from Bogoslof was a small steam plume from a subaerial vent observed on 14 December (event 3; Coombs et al. 2019), shortly after an episode of earthquakes merging into tremor (P2). Late on 15 December, noise levels on station MAPS increased substantially, making it difficult to determine the end of this phase.

16 December 2016 to 13 March 2017 – Explosive Phase I:
On or around 16 December, the Opening Phase gave way to the first phase of explosive eruptions. Explosions occurred roughly every other day for the first two months, becoming more sparse starting in mid-February. Of the 70 numbered explosions, 35 occurred in this phase. During Explosive Phase I, around half of all explosions were preceded by earthquakes that increased in rate before merging into tremor that led into the explosion (Figure 5a; Tepp and Haney 2019), which was useful for short-term forecasting (Coombs et al. 2018). The last explosion in this phase (event 38) was preceded by earthquake swarms (S5, S6, and P14) occurring

over ~3.5 days. The December lava dome also first became visible in satellite images during this phase, although it is unclear whether it began being extruded earlier (Waythomas et al. 2019).

14 March to 16 May 2017 – Eruption Pause:
A 2-month pause in eruptive activity followed the explosion on 13 March (event 38). Very little seismicity was detected during this pause. A lone swarm (S7) lasting ~3 hours on 15-16 April was the only significant activity. This swarm is interpreted as an intrusion below the volcanic edifice. Daily AVO satellite reports from this period indicate only a few days with thermal anomalies, which were typically weak and likely related to a warm lagoon (Coombs et al. 2019), indicating an accompanying pause in surficial activity.

17 May to 30 August 2017 – Explosive Phase II:
Explosive activity renewed on 17 May (event 39) and included the remaining 32 numbered explosions. However, the character of Explosive Phase II was typically different than Explosive Phase I. The seismically-detectable accelerating earthquakes were not observed during this phase (Supplementary Material S2); however, a weak accelerating swarm (HP2) and an accelerating RRE swarm (HP7b) were identified in the hydrophone data (Table 4). There were 3 major swarms seismically detected (Table 3; Figure 11): a swarm that preceded the 1 June explosion (event 41) by ~4.5 hours (P15), the tremor swarm (T1) on 1 Jul, and a swarm on 15 August (S8) that was likely produced by a magma intrusion. Additionally, the hydrophone detected 14 swarms of weak earthquakes that preceded explosions by a few hours or less (Supplementary Material S3). Explosive Phase II also included the construction and subsequent destruction of two lava domes (e.g., Waythomas et al. 2019). Neither of these lava domes had seismicity clearly associated with their growth. A few explosions occurred during the emplacement of each. These explosions tended to lack seismic precursors (Tepp and Haney 2019), have a smaller tremor magnitude (Figure 8), and sometimes have higher peak frequencies in infrasound (Lyons et al. 2019). These characteristics are suggestive of surficial phreatomagmatic explosions from water interacting with the growing lava domes. Seismic activity from the Bogoslof eruption concluded with an explosion on 30 August (event 70) and a few sporadic earthquakes through the next day. Steaming and weak fumarolic activity were observed up through a field visit in August 2018 and in later satellite images (e.g., Coombs et al. 2019), although this is from residual heat rather than new eruptive activity. A local seismic station (BOGO) deployed on Bogoslof Island during the August 2018 visit has not recorded any notable activity.

Summary

Bogoslof volcano erupted from December 2016 through August 2017, with precursory seismic activity primarily beginning in September 2016. The eruption comprised 70 major explosive eruptions, around 76 earthquake swarms, over 3200 earthquakes, and 3 lava domes. As Bogoslof is unmonitored, the eruption seismicity was only recorded in real-time on regional seismic and infrasound networks. However, detection was good enough to allow for timely response efforts and good characterization of the eruption. A local hydrophone deployed during the second half of the eruption provided additional detail of the seismic activity. Few emergent eruptions have been recorded seismo-acoustically, with the 2016-17 Bogoslof eruption having arguably the best seismo-acoustic recordings of any such eruption of this type.

The eruption produced a variety of seismicity, including earthquakes, seismic swarms, non-eruptive tremor, and co-eruptive tremor and earthquakes. However, no seismicity associated with lava dome growth could be confidently identified. The earthquakes had a variety of characteristics and recorded phases. Most of the earthquakes occurred in 74 swarms, 27 of which comprised small earthquakes that were only detectable by the local hydrophone. The explosion seismicity was dominated by tremor but also often included co-eruptive earthquakes. Tremor magnitudes and frequency content of explosions were fairly consistent throughout the eruption, except for explosions that occurred while the June and August lava domes were emplaced which tended to have smaller magnitudes. Tremor magnitudes determined from the hydrophone data show a roughly linear relation to plume heights. However, the seismic data shows no clear trend, suggesting that the relation may be applicable only to the summer months or perhaps only to the hydrophone recordings. Three cases of precursory gliding tremor were observed along with a case of gliding harmonic tremor associated with unidentified activity. The hydrophone recorded a diffuse, broad-band, noise-like signal after 4 explosions that was likely produced by a mass flow event.

Seismically, the Bogoslof eruption can be broken into five different phases. The Precursory Phase included the initial increase in seismicity with a swarm from a magma intrusion in late September 2016 and more earthquakes continuing into October. After about two months of only occasional sporadic earthquakes, the Opening Phase of the eruption occurred in mid-December, ending with the earliest observed possible explosions. This phase was defined by earthquakes merging into and out of tremor almost continuously. Explosive Phase I progressed until mid-March 2017 and included most of the seismically detected earthquake swarms. Around half of the explosions in this phase were preceded by earthquake swarms with an accelerating rate that were useful for short-term forecasting. From mid-March to mid-May, the eruption paused with no significant surficial activity and only a single swarm, likely related to magma intrusion, detected in mid-April. The pause was followed by Explosive Phase II which continued until the eruption ended in late August 2017. There have been no further signs of eruptive activity since then, though local, regional, and satellite monitoring of Bogoslof continues.

References

Bohnenstiehl, D. R., Dziak, R. P., Matsumoto, H., & Lau, T. K. A. (2013). Underwater acoustic records from the March 2009 eruption of Hunga Ha'apai-Hunga Tonga volcano in the Kingdom of Tonga. Journal of Volcanology and Geothermal Research, 249, 12-24.

Buurman, H. & West, M.E. (2010). Seismic precursors to volcanic explosions during the 2006 eruption of Augustine Volcano. *The 2006 eruption of Augustine Volcano, Alaska*, edited by Power, J.A., Coombs, M.L., and Freymueller, J.T. *U.S. Geological Survey Professional Paper,* 1769, 41–57.

Buurman, H., West, M. E., & Thompson, G. (2013). The seismicity of the 2009 Redoubt eruption. Journal of Volcanology and Geothermal Research, 259, 16-30. doi: 10.1016/j.jvolgeores.2012.04.024.

Carey, W. M. (2009). Lloyd's mirror-image interference effects. Acoust. Today, 5(2), 14-20.

Coombs, M. L., Wech, A., Haney, M., Lyons, J., Schneider, D. J., Schwaiger, H., Wallace, K., Fee, D., Freymueller, J., Schaefer, J., & Tepp, G. (2018). Short-term forecasting and detection of explosions during the 2016–2017 eruption of Bogoslof volcano, Alaska. Frontiers in Earth Science, 6, 122.

Coombs, M. L., Wallace, K., Cameron, C., Angeli, K., & Cervelli, P. (2019). Overview, chronology, and impacts of the 2016-2017 eruption of Bogoslof volcano. Bulletin of Volcanology.

Dietz, R. S., & Sheehy, M. J. (1954). Transpacific detection of Myojin volcanic explosions by underwater sound. Geological Society of America Bulletin, 65(10), 941-956.

Drobiarz, Jonathan G. (2017). "Interpreting the dynamics of submarine landslides through hydroacoustic modeling, West Mata volcano, NE Lau Basin". Western Washington University Masters Thesis Collection, 593.

Dziak, R. P., & Fox, C. G. (2002). Evidence of harmonic tremor from a submarine volcano detected across the Pacific Ocean basin. Journal of Geophysical Research: Solid Earth, 107(B5), ESE 1-11. doi: 10.1029/2001JB000177.

Fee, D., Lyons, J. J., Haney, M. M., Wech, A., Waythomas, C., Diefenbach, A., Lopez, T., Van Eaton, A., & Schneider, D. (2019). Seismo-acoustic evidence for vent drying during shallow submarine eruptions at Bogolsof volcano, Alaska. Bulletin of Volcanology.

Green, D. N., Evers, L. G., Fee, D., Matoza, R. S., Snellen, M., Smets, P., & Simons, D. (2013). Hydroacoustic, infrasonic and seismic monitoring of the submarine eruptive activity and sub-aerial plume generation at South Sarigan, May 2010. Journal of Volcanology and Geothermal Research, 257, 31-43. doi: 10.1016/j.jvolgeores.2013.03.006.

Haney, M. M., Fee, D., McKee, K. F., Lyons, J. J., Matoza, R. S. Wech A. G., Tepp, G. Searcy, C., and Mikesell, T. D. (2019a). Co-eruptive tremor from Bogoslof Volcano, Alaska: Seismic wavefield composition at regional distances. Bull. Volc.

Haney, M. M., Van Eaton, A. R., Lyons, J. J., Kramer, R. L., Fee, D., Iezzi, A. M., Dziak, R. P., Anderson, J., Johnson, J. B., & Lapierre, J. L. (2019b). Characteristics of thunder and electromagnetic pulses from volcanic lightning at Bogoslof Volcano, Alaska. Bull. Volc.

Haxel, J. H., Dziak, R. P. & Matsumoto, H. (2013). Observations of shallow water marine ambient sound: The low frequency underwater soundscape of the central Oregon coast. The Journal of the Acoustical Society of America, 133, 2586–2596.

Hotovec, A. J., Prejean, S. G., Vidale, J. E., & Gomberg, J. (2013). Strongly gliding harmonic tremor during the 2009 eruption of Redoubt Volcano. Journal of Volcanology and Geothermal Research, 259, 89-99. doi: 10.1016/j.jvolgeores.2012.01.001.

Iverson, R. M., Dzurisin, D., Gardner, C. A., Gerlach, T. M., LaHusen, R. G., Lisowski, M., Major, J. J., Malone, S. D., Messerich, J. A., Moran, S. C., & Pallister, J. S. (2006). Dynamics of seismogenic volcanic extrusion at Mount St Helens in 2004–05. Nature, 444(7118), 439.

Johnson, R. H., & Norris, R. A. (1972). Significance of spectral banding in hydroacoustic signals from submarine volcanic eruptions: Myojin, 1970, J. Geophys. Res., 77(23), 4461–4469, doi:10.1029/JB077i023p04461.

Ketner, D., & Power, J. (2013). Characterization of seismic events during the 2009 eruption of Redoubt Volcano, Alaska. Journal of Volcanology and Geothermal Research, 259, 45-62.

Kutschale, H. (1969). Arctic hydroacoustics. Arctic, 22(3), 246-264.

Loewen, M. W., Izbekov, P. , Moshrefzadeh, J., Coombs, M., Larsen, J., Graham N., Harbin, M., Waythomas, C., & Wallace, K. (2019). Petrology of the 2016-2017 eruption of Bogoslof Island, Alaska. Bulletin of Volcanology.

Lopez, T., Clarisse, L., Schwaiger, H. F., Van Eaton, A. R., Loewen, M. W., Fee, D., Lyons, J. J., Haney, M. M., Wallace, K. L., Searcy, C., Wech, A. G., Schneider, D. J., Graham, N. (2019). Constraints on eruption processes and event masses for the 2016-2017 eruption of Bogoslof volcano, Alaska, through evaluation of IASI satellite SO2 masses and complementary datasets. Bulletin of Volcanology.

Lyons, J. J., Fee, D., Haney, M. M., & Iezzi, A. (2019). Infrasound generated by the shallow submarine eruption of Bogoslof volcano, Alaska. Bulletin of Volcanology.

Machado, F., Parsons, W. H., Richards, A. F., and Mulford, J. W. (1962). Capelinhos eruption of Fayal Volcano, Azores, 1957–1958. J. Geophys. Res., 67(9), 3519–3529, doi:10.1029/JZ067i009p03519.

McNutt, S. R. (2005). Volcanic seismology. Annu. Rev. Earth Planet. Sci., 32, 461-491.

Metz, D., Watts, A. B., Grevemeyer, I., Rodgers, M., & Paulatto, M. (2016). Ultra-long-range hydroacoustic observations of submarine volcanic activity at Monowai, Kermadec Arc. Geophys. Res. Lett., 43, 1529–1536. doi:10.1002/2015GL067259.

Neuberg, J., Luckett, R., Baptie, B., & Olsen, K. (2000). Models of tremor and low-frequency earthquake swarms on Montserrat. Journal of Volcanology and Geothermal Research, 101(1-2), 83-104. doi: 10.1016/S0377-0273(00)00169-4.

Nishi, K. (1974). Relation between micro-earthquake swarm and explosion earthquakes at Sakurajima volcano. Abstracts of Natural Disaster Science Symposium, 11, 345-346, (in Japanese).

Powell, T. W., & Neuberg, J. (2003). Time dependent features in tremor spectra. *Journal of Volcanology and Geothermal Research*, *128*(1-3), 177-185. doi: 10.1016/S0377-0273(03)00253-1.

Richards, A. F. (1963), Volcanic sounds: Investigation and analysis, J. Geophys. Res., 68(3), 919–928, doi:10.1029/JZ068i003p00919.

Schneider, D., Van Eaton, A., & Wallace, K. (2019). Satellite Observations of the 2016-17 Eruption of Bogoslof volcano: Aviation and Ash Fallout Hazard Implications from a Water-Rich Eruption. Bulletin of Volcanology.

Schöpa, A., Chao, W. A., Lipovsky, B. P., Hovius, N., White, R. S., Green, R. G., & Turowski, J. M. (2018). Dynamics of the Askja caldera July 2014 landslide, Iceland, from seismic signal analysis: precursor, motion and aftermath. Earth Surface Dynamics, 6(2), 467-485. Doi: 10.5194/esurf-6-467-2018.

Searcy, C. (2013). Seismicity associated with the May 2010 eruption of South Sarigan Seamount, northern Mariana Islands. Seismological Research Letters, 84(6), 1055-1061. doi: 10.1785/0220120168.

Searcy, C. K. & Power, J. A. (2009). Progression and character of explosive activity during the 2016/17 eruption of Bogoslof volcano, Alaska. Bulletin of Volcanology.

Smink, M. (2017). ‘Evanescent wave coupling’ between the ocean and atmosphere by use of infrasound and hydroacoustic data generated by the Hunga Tonga underwater volcano eruption of 2014-2015, Master’s Thesis, Koninklijk Nederlands Meteorologisch Instituut, 85p.

Talandier, J. (2004). Seismicity of the Society and Austral hotspots in the South Pacific: Seismic detection, monitoring and interpretation of underwater volcanism. In Oceanic Hotspots (pp. 29-71). Springer, Berlin, Heidelberg.

Tameguri, T., & Iguchi, M. (2019). Characteristics of micro-earthquake swarms preceding eruptions at Showa crater of Sakurajima volcano, Japan. Journal of Volcanology and Geothermal Research, 372, 24-33. doi: 10.1016/j.jvolgeores.2019.01.016.

Tepp, G. (2018). A Repeating Event Sequence Alarm for Monitoring Volcanoes. Seismological Research Letters, 89(5), 1863-1876, doi:10.1785/0220170263.

Tepp, G. & Haney, M. (2019). Comparison of short-term seismic precursors and explosion parameters during the 2016-17 Bogoslof eruption. Bulletin of Volcanology.

Tepp, G., Chadwick, W. W., Haney, M. M., Lyons, J. J., Dziak, R. P., Merle, S. G., Butterfield, D. A., and Young, C. W. (2019). Hydroacoustic, Seismic, and Bathymetric Observations of the 2014 Submarine Eruption at Ahyi Seamount, Mariana Arc. Geochemistry, Geophysics, Geosystems. Doi:10.1029/2019GC008311.

Thelen, W., Malone, S., & West, M. (2011). Multiplets: Their behavior and utility at dacitic and andesitic volcanic centers. Journal of Geophysical Research: Solid Earth, 116(B8).

Thompson, G., & Reyes, C. (2018). GISMO – a seismic data analysis toolbox for MATLAB [software package], http://geoscience-community-codes.github.io/GISMO/, Accessed February 2018.

Thompson, G., & West, M. E. (2010). Real-time detection of earthquake swarms at Redoubt Volcano, 2009. Seismological Research Letters, 81(3), 505-513.

Van Eaton, A., Schneider, D. J., Smith, C. M., Haney, M. M., Lyons, J. J., Said, R., Fee, D., & Holzworth, R. H. (2019). Ice charging generates volcanic lightning during the 2016–2017 Surtseyan eruption of Bogoslof, Alaska. Bulletin of Volcanology.

Waythomas, C. F., & Cameron, C. E. (2018). Historical eruptions and hazards at Bogoslof volcano, Alaska. U.S. Geological Survey Scientific Investigations Report 2018–5085, 42 p. doi: 10.3133/sir20185085.

Waythomas, C., Angeli, K., Wessels, R., & Schneider, D. (2019). 2016-17 evolution of the submarine-subaerial edifice of Bogoslof volcano, Alaska, based on analysis of satellite imagery. Bulletin of Volcanology.

Wech, A., Tepp, G., Lyons, J., & Haney, M. (2018). Using earthquakes, *T* waves, and infrasound to investigate the eruption of Bogoslof volcano, Alaska. *Geophysical Research Letters*, 45, 6918– 6925.

White, R. A., Miller, A. D., Lynch, L., & Power, J. (1998). Observations of hybrid seismic events at Soufriere Hills volcano, Montserrat: July 1995 to September 1996, Geophysical Research Letters, 25, no. 19, 3657-3660, doi: 10.1029/98GL02427.

Figure and Table Captions

Figure 1: Regional map showing Bogoslof (red triangle) and nearby instruments. Blue and blue-green circles indicate stations with broad-band and short-period seismometers, respectively. The white circle marks the hydrophone location. Inset shows the location of Bogoslof in Alaska and other places mentioned in the text.

Figure 2: Diagrams of the hydrophone mooring and hydroacoustic sound speed profiles. (a) Vertically-exaggerated Bogoslof profile with a diagram of the hydrophone mooring (not to scale) at its approximate location. (b) Approximate sound speed profiles calculated from PFL data recorded in the summer of 2007 in (c) several different locations around Bogoslof. Colors of lines and circles in (b) and (c) correspond to the same days. Circles are labeled with the UTC time that the data were recorded. The red triangle indicates the location of Bogoslof. The white star marks the hydrophone location.

Figure 3: 30 June 2017 eruption sequence recorded on, from top to bottom, the hydrophone (7 km), an Umnak seismometer (53 km), an Unalaska seismometer (73 km), and 3 seismometers on Tanaga Island (~700 km). The onsets of the earthquake, glide, and eruption tremor are marked by white dashed lines on the top spectrogram. All 3 events are visible on the 3 Tanaga stations. On TANO, the reflected phase is stronger than the direct arrival and arrives ~1.5 min later.

Figure 4: Example waveforms of different earthquake types recorded on (a) & (b) the vertical component of seismic station MAPS and (c) the hydrophone. Amplitudes are normalized. Approximate phase arrivals are marked by red dashed lines and labeled. P and S are direct body-wave arrivals. Pr is the Moho-reflected phase, and T

is the converted hydroacoustic phase. T1 and T2 mark the first and second arrivals on the hydrophone. UTC times are given for the waveform start.

Figure 5: Examples of seismic swarms: (a) precursory swarm merging into tremor, (b) post-eruptive swarm (explosion tremor visible during first ~6 min), (c) general earthquake swarm, (d) tremor swarm, and (e) mid-December swarm. Waveform data were filtered from 2.5-10 Hz. Note that these examples do not show the full duration of the swarms.

Figure 6: Sequence statistics for the 41 swarms based on the matched filter catalog: (a) swarm duration histogram, (b) average earthquake rate histogram, (c) maximum earthquake rate compared to swarm duration, (d) maximum earthquake rate histogram, (e) number of earthquakes compared to swarm duration, and (f) histogram showing the number of earthquakes in the swarm. Precursory (red), post-eruptive (blue), and general (black) categories refer to the presence of an explosion occurring within 4.5 hours before a swarm start (precursory) or within 4.5 hours after a swarm end (post-eruptive) or the lack of relation to explosions (general).

Figure 7: Sequence statistics for the 18 swarms determined from the hydroacoustic matched filter catalog: (a) swarm duration histogram, (b) average earthquake rate histogram, (c) maximum earthquake rate compared to swarm duration, (d) maximum earthquake rate histogram, (e) number of earthquakes compared to swarm duration, and (f) histogram showing the number of earthquakes in the swarm. Precursory (red), post-eruptive (blue), and general (black) categories refer to the presence of an explosion occurring within 4.5 hours before a swarm start (precursory) or within 4.5 hours after a swarm end (post-eruptive) or the lack of relation to explosions (general).

Figure 8: Plots showing (a) duration, (b) tremor magnitude, (c) frequency index, and (d) average frequency for each explosion over the duration of the eruption. (e) Comparison of tremor magnitudes determined from seismic (MAPS, red and OKER, white) and hydroacoustic data. (f) Comparison of tremor magnitudes to plume heights (Schneider et al. 2019). In (a), the red circles represent durations from the seismic stations and blue triangles from the hydrophone. For (b)-(f), red circles are measurements made on seismic station MAPS, white circles on seismic station OKER, and blue triangles on hydrophone HC09. Blue triangles are shaded by amount of clipping: dark is none, mid is minor, and light is major. Gray bars indicate the approximate duration of lava domes that were produced and destroyed during the eruption.

Figure 9: Spectrograms of the 2 Jul 2017 post-eruptive sequence starting at 21:26:30. The top spectrogram is from the hydrophone, and the bottom two are from regional seismometers.

Figure 10: Spectrograms of explosions and post-eruptive diffuse signals recorded in hydroacoustic (top) and seismic (bottom) data on a) 24 June, b) 27 June, c) 5 July, and d) 27 August 2017. Note that the 27 August explosion had significant clipping (strong broad-band lines).

Figure 11: Eruption timeline showing normalized RMS amplitude, daily earthquake counts, explosions, and eruption phases. RMS amplitude was calculated using 12-hour windows with 3 hours of overlap and normalized for each channel separately. Seismic data were filtered between 2-15 Hz. Hydroacoustic data were filtered between 2-75 Hz. Red, yellow, and blue indicate RMS amplitude measured on MAPS, OKER, and HC09, respectively. Red and blue bars show the daily earthquake counts from the matched-filter catalogs of MAPS (left axis) and HC09 (right axis), respectively. Major seismic swarms are labeled. Explosions are shown as gray vertical lines at the onset time, and eruption phases are divided by black vertical lines.

Table 1: Seismic & Hydroacoustic Observations of Near or At Sea-surface Eruptions

Table 2: Seismic Station Information and Data Return
* Data return for one year starting 1 September 2016. For analog short-period stations, data return is estimated as the percentage of calibration pulses, sent once every 12 hours, that are returned with the proper ID.

Table 3: Major Seismic Swarms
* Swarms are numbered with a letter followed by a number: P=precursory, S=general swarm, A=post-eruptive ("after"), T=tremor
** “un” signifies an explosion that was unnumbered in the catalog of Coombs et al. (2019)

Table 4: Major Hydroacoustically-recorded Swarms
* Swarms are numbered with an “H” to indicate hydroacoustically-recorded and a letter followed by a number: P=precursory, S=general swarm, A=post-eruptive ("after"), T=tremor
** “un” signifies an explosion that was unnumbered in the catalog of Coombs et al. (2019)

Table 5: Major Co-eruptive Earthquake Swarms

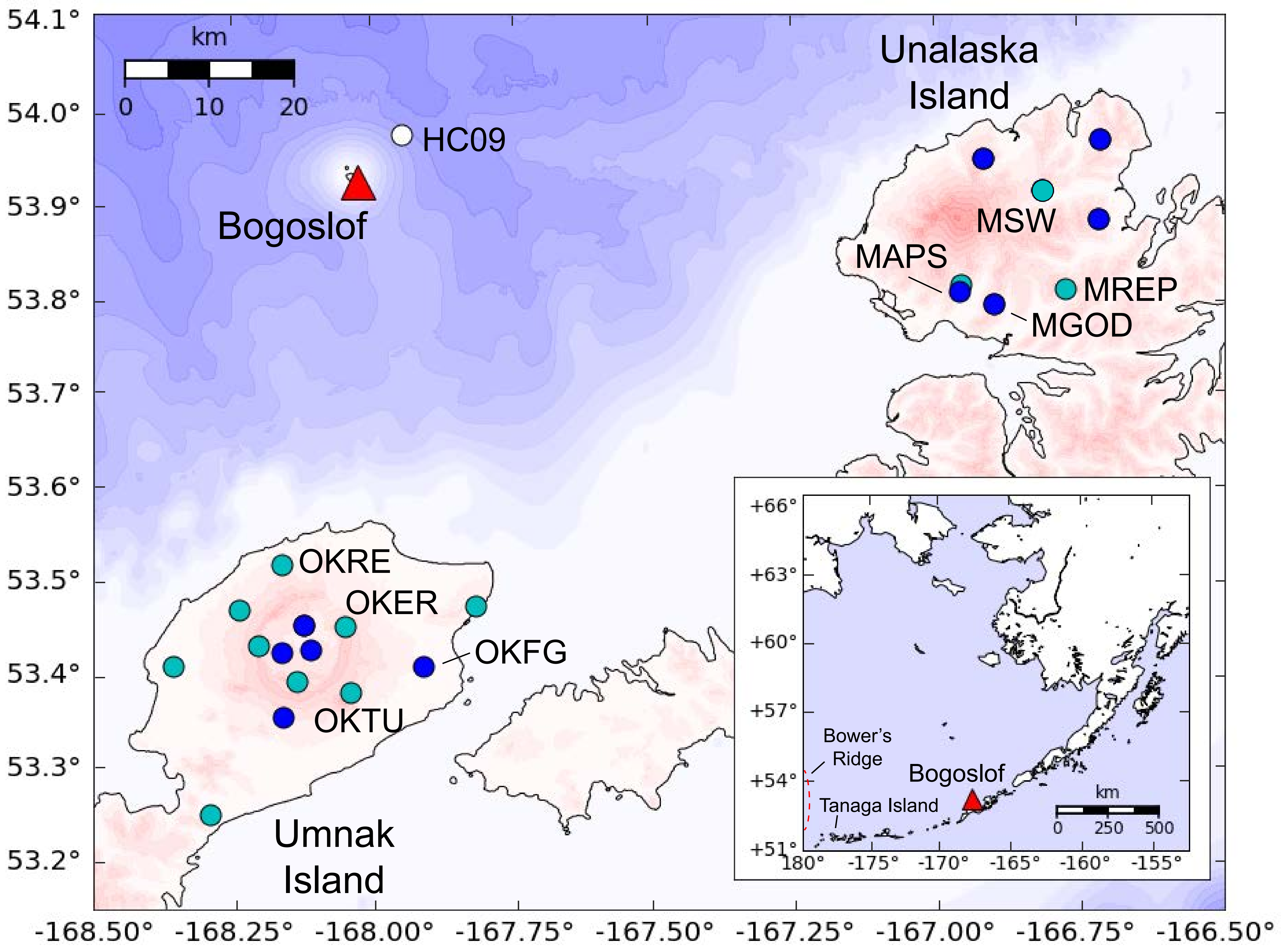

km
0
10
20
HC09
Bogoslof
Unalaska
Island
MSW
MAPS
MREP
MGOD
OKRE
OKER
OKFG
OKTU
Umnak
Island
Bower's
Ridge
Bogoslof
Tanaga Island
km
0
250
500
+66°
+63°
+60°
+57°
+54°
+51°
180°
-175°
-170°
-165°
-160°
-155°
54.1°
54.0°
53.9°
53.8°
53.7°
53.6°
53.5°
53.4°
53.3°
53.2°
-168.50°
-168.25°
-168.00°
-167.75°
-167.50°
-167.25°
-167.00°
-166.75°
-166.50°

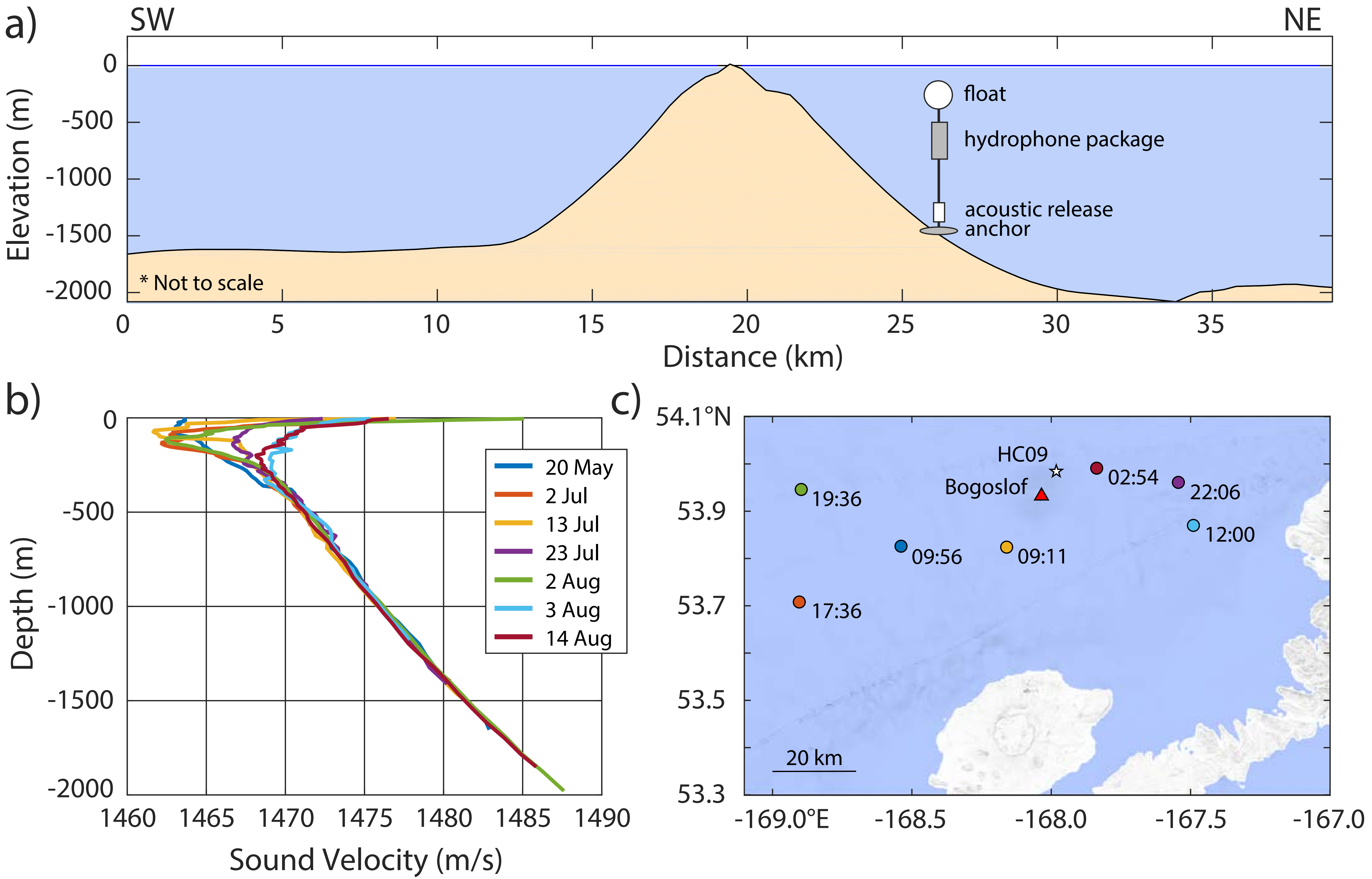

a)
SW
NE
Elevation (m)
0
-500
-1000
-1500
-2000
float
hydrophone package
acoustic release
anchor
* Not to scale
0
5
10
15
20
25
30
35
Distance (km)
b)
Depth (m)
Sound Velocity (m/s)
1460
1465
1470
1475
1480
1485
1490
20 May
2 Jul
13 Jul
23 Jul
2 Aug
3 Aug
14 Aug
c)
54.1°N
53.9
53.7
53.5
53.3
-169.0°E
-168.5
-168.0
-167.5
-167.0
HC09
Bogoslof
02:54
22:06
19:36
12:00
09:56
09:11
17:36
20 km

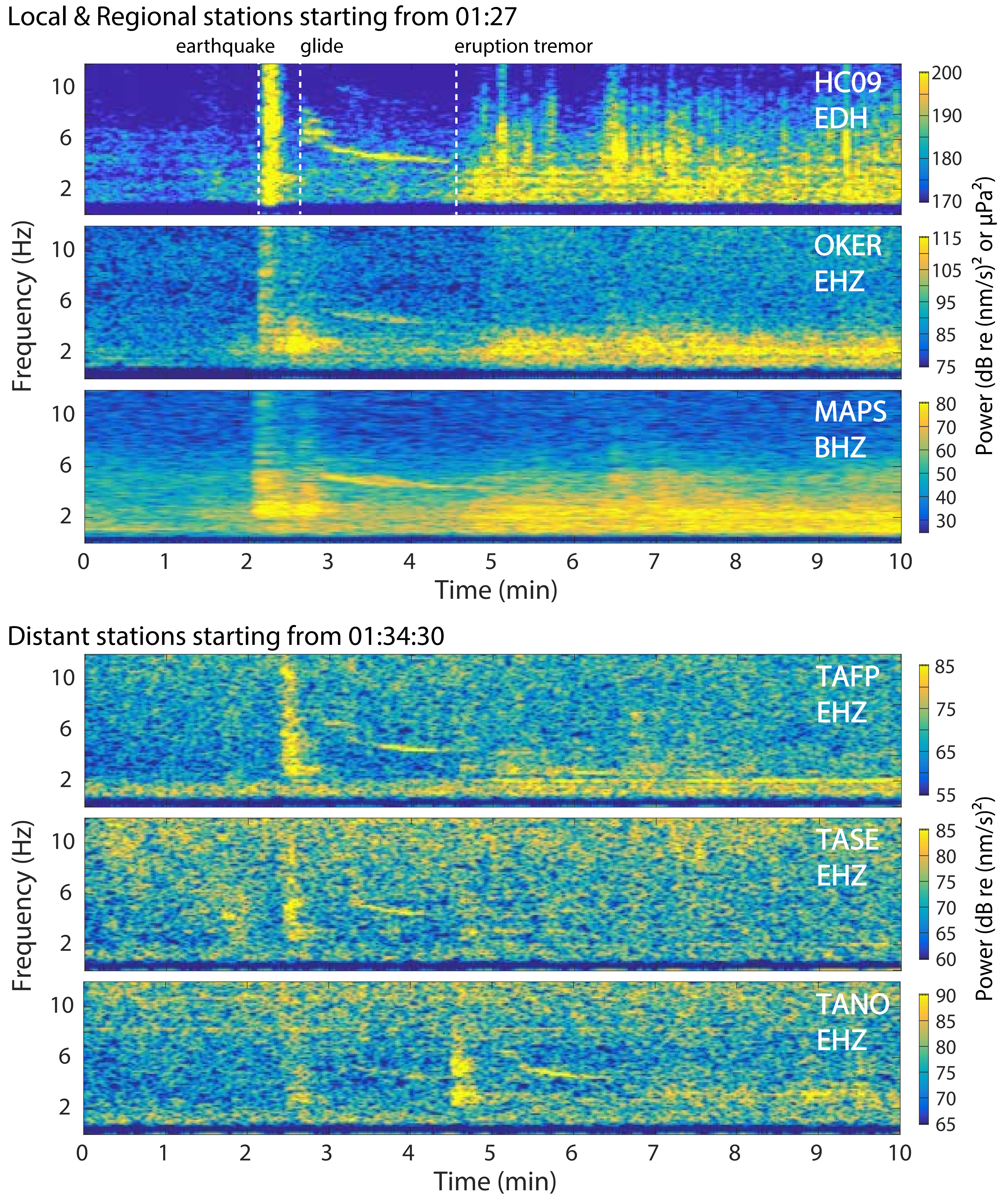

Local & Regional stations starting from 01:27
earthquake
glide
eruption tremor
HC09
EDH
OKER
EHZ
MAPS
BHZ
Frequency (Hz)
Power (dB re (nm/s)^2 or μPa^2)
Time (min)
Distant stations starting from 01:34:30
TAFP
EHZ
TASE
EHZ
TANO
EHZ
Frequency (Hz)
Power (dB re (nm/s)^2)
Time (min)

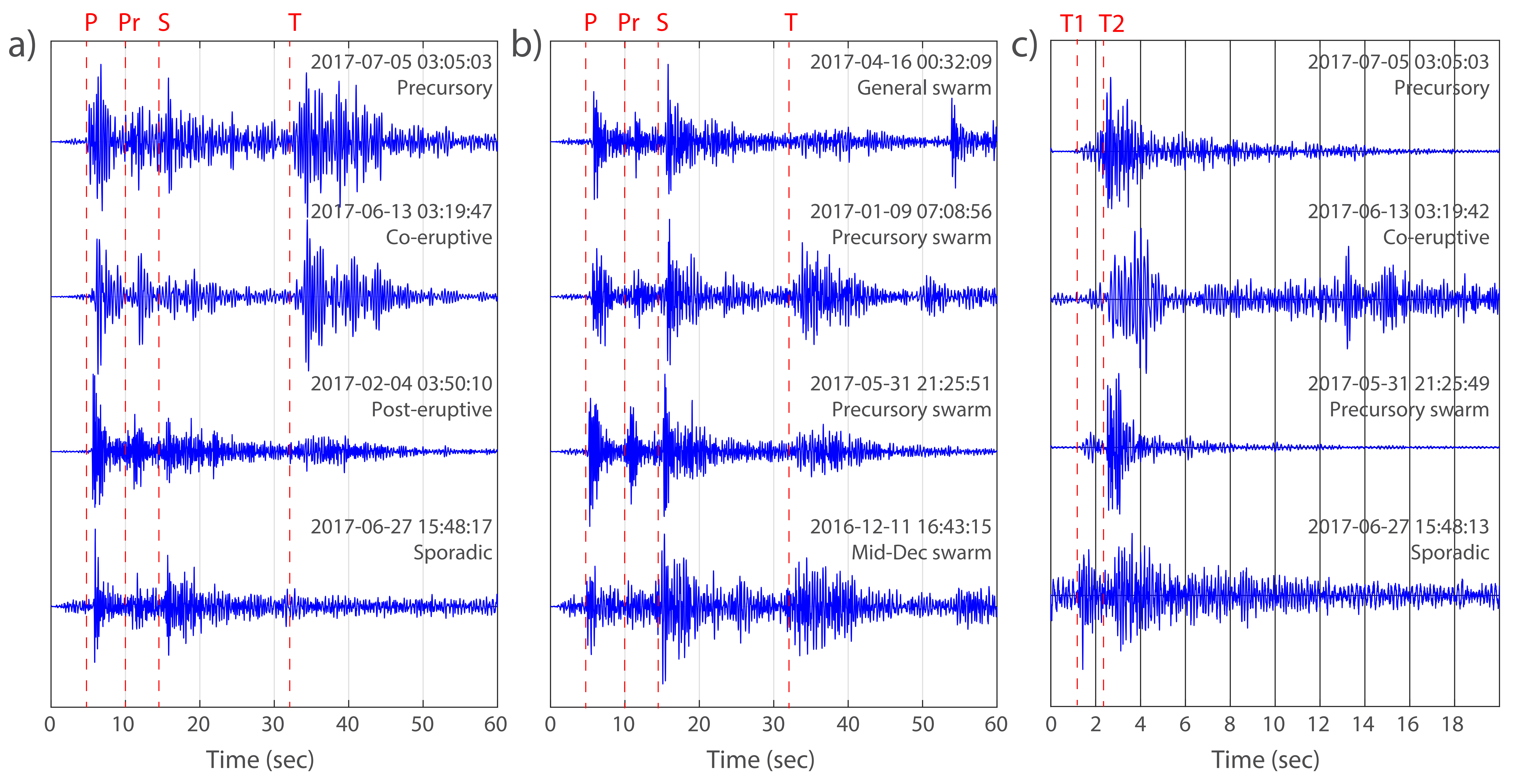

a)
P
Pr
S
T
2017-07-05 03:05:03
Precursory
2017-06-13 03:19:47
Co-eruptive
2017-02-04 03:50:10
Post-eruptive
2017-06-27 15:48:17
Sporadic
0
10
20
30
40
50
60
Time (sec)
b)
P
Pr
S
T
2017-04-16 00:32:09
General swarm
2017-01-09 07:08:56
Precursory swarm
2017-05-31 21:25:51
Precursory swarm
2016-12-11 16:43:15
Mid-Dec swarm
0
10
20
30
40
50
60
Time (sec)
c)
T1
T2
2017-07-05 03:05:03
Precursory
2017-06-13 03:19:42
Co-eruptive
2017-05-31 21:25:49
Precursory swarm
2017-06-27 15:48:13
Sporadic
0
2
4
6
8
10
12
14
16
18
Time (sec)

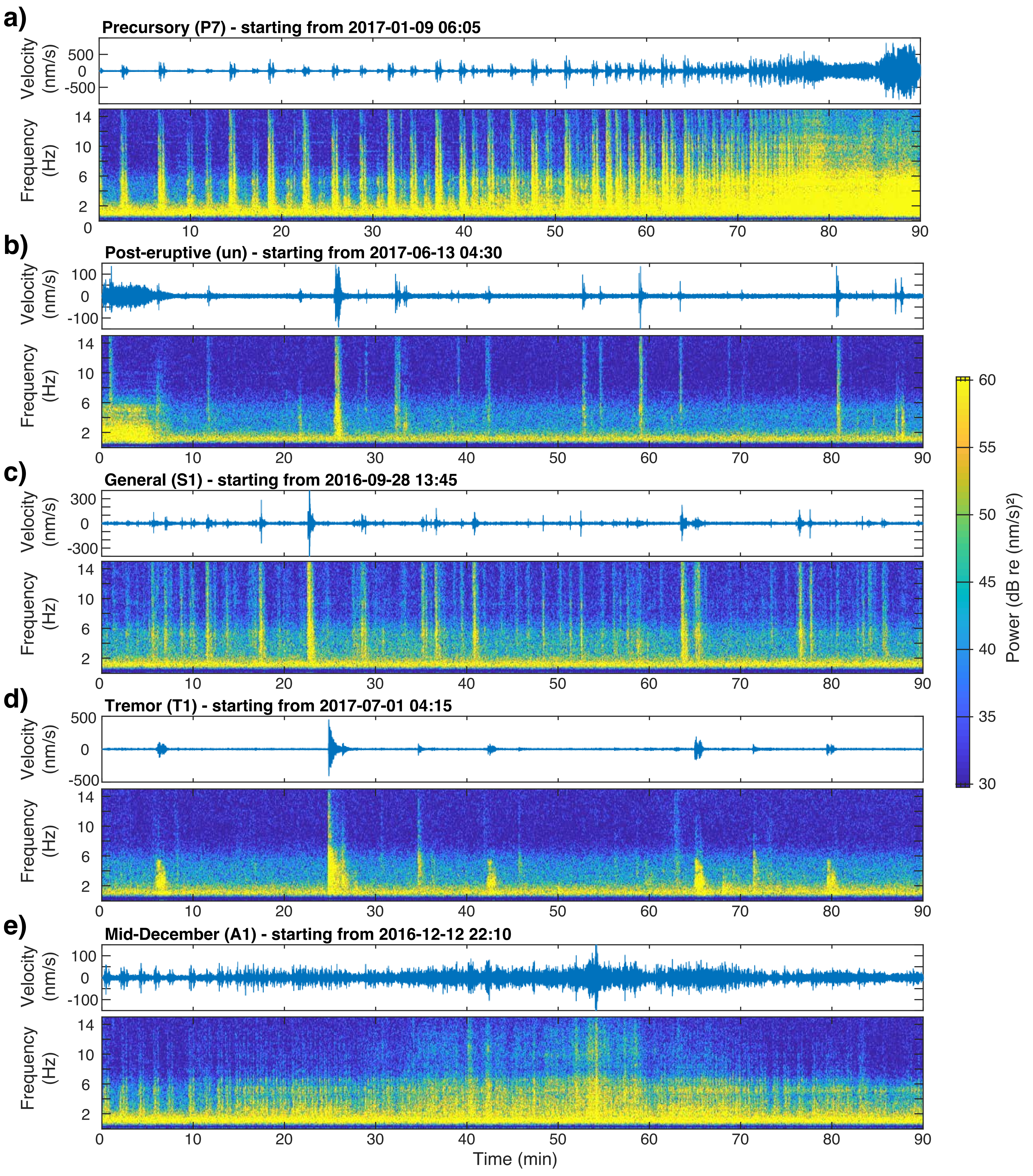

a)
Precursory (P7) - starting from 2017-01-09 06:05
b)
Post-eruptive (un) - starting from 2017-06-13 04:30
c)
General (S1) - starting from 2016-09-28 13:45
d)
Tremor (T1) - starting from 2017-07-01 04:15
e)
Mid-December (A1) - starting from 2016-12-12 22:10
Velocity (nm/s)
Frequency (Hz)
Time (min)
Power (dB re (nm/s)²)

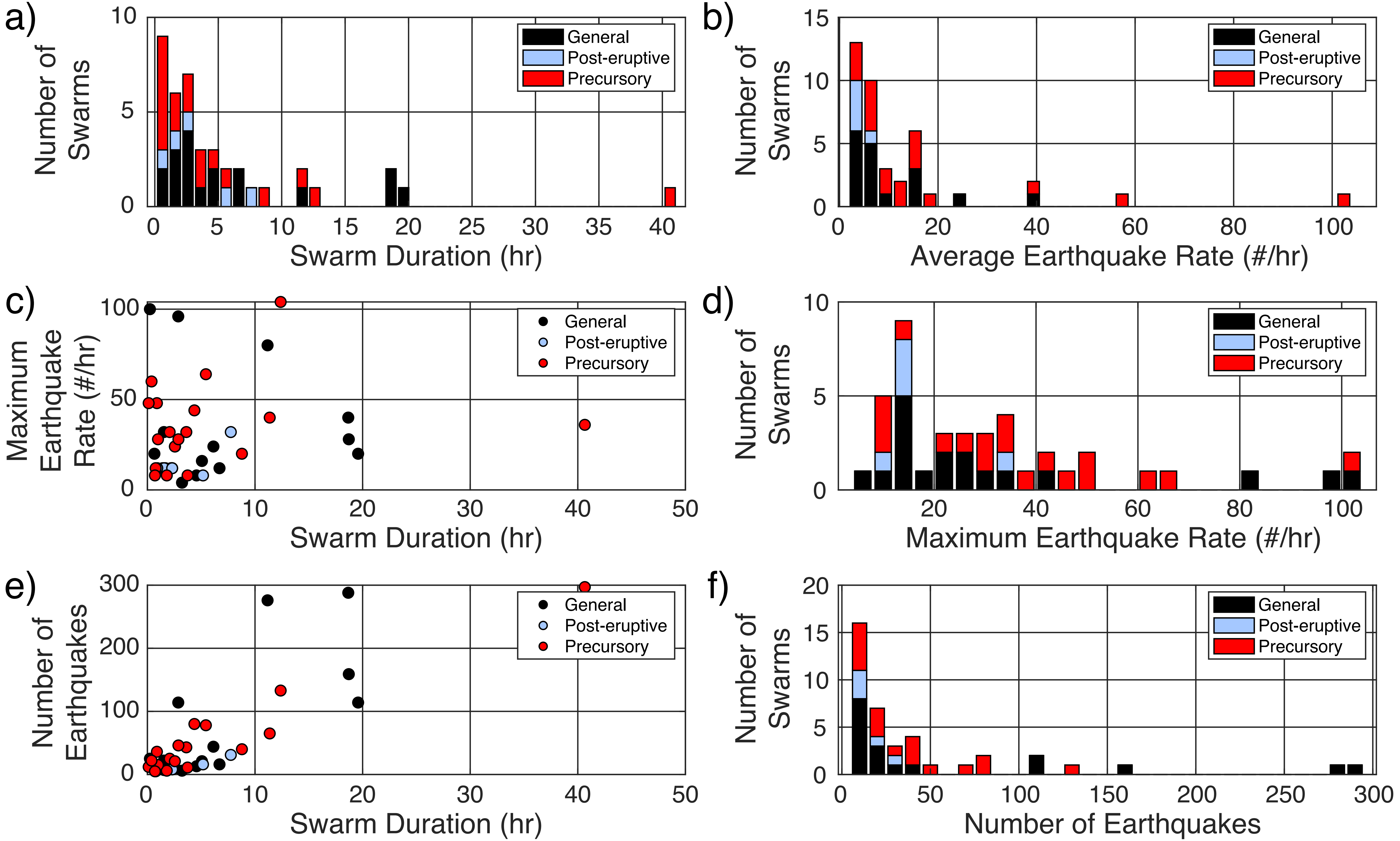

a)
Number of Swarms
Swarm Duration (hr)
General
Post-eruptive
Precursory
b)
Number of Swarms
Average Earthquake Rate (#/hr)
c)
Maximum Earthquake Rate (#/hr)
Swarm Duration (hr)
d)
Number of Swarms
Maximum Earthquake Rate (#/hr)
e)
Number of Earthquakes
Swarm Duration (hr)
f)
Number of Swarms
Number of Earthquakes

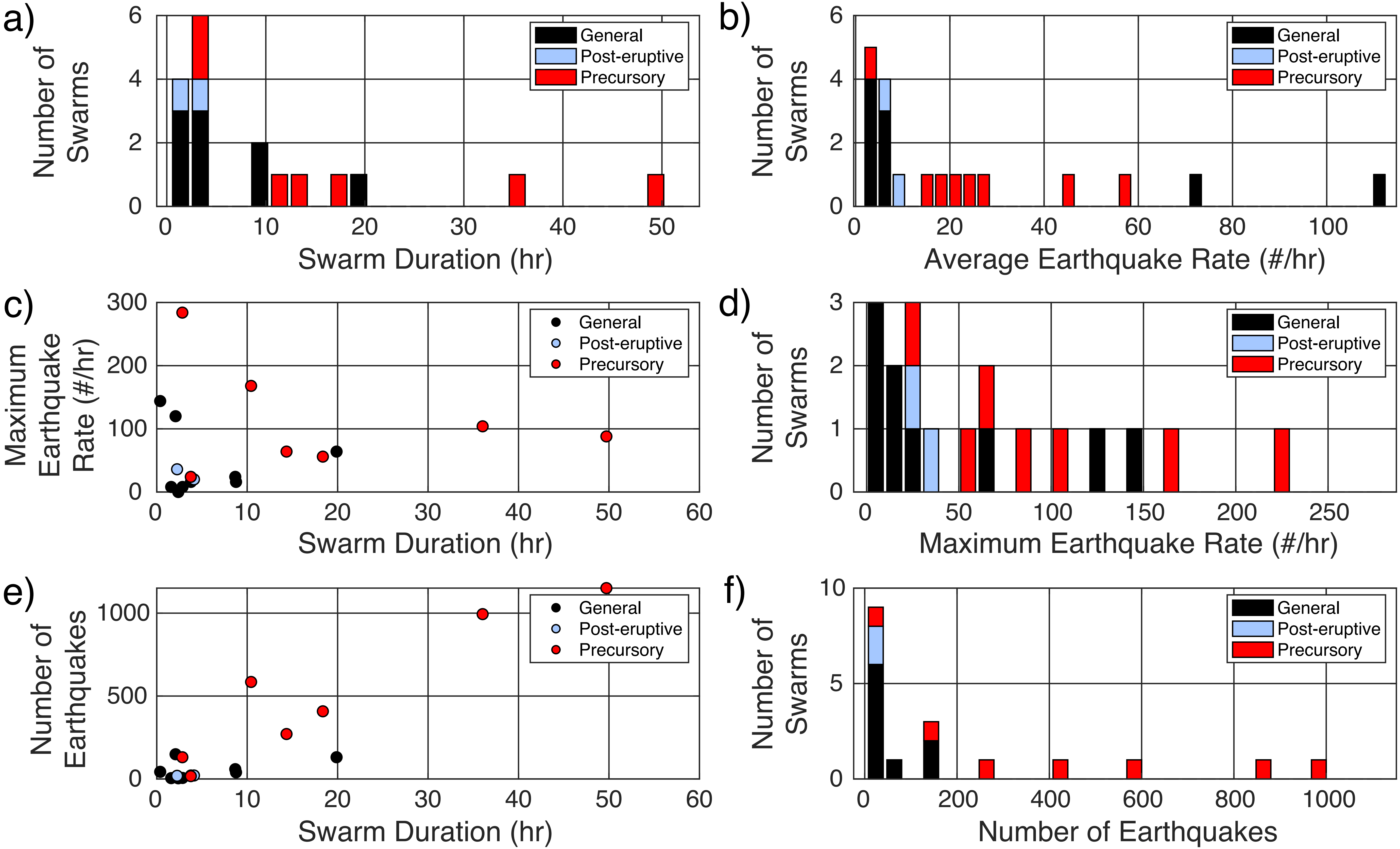
a)
b)
c)
d)
e)
f)
Number of Swarms
Swarm Duration (hr)
Average Earthquake Rate (#/hr)
Maximum Earthquake Rate (#/hr)
Maximum Earthquake Rate (#/hr)
Number of Earthquakes
Number of Earthquakes
General
Post-eruptive
Precursory

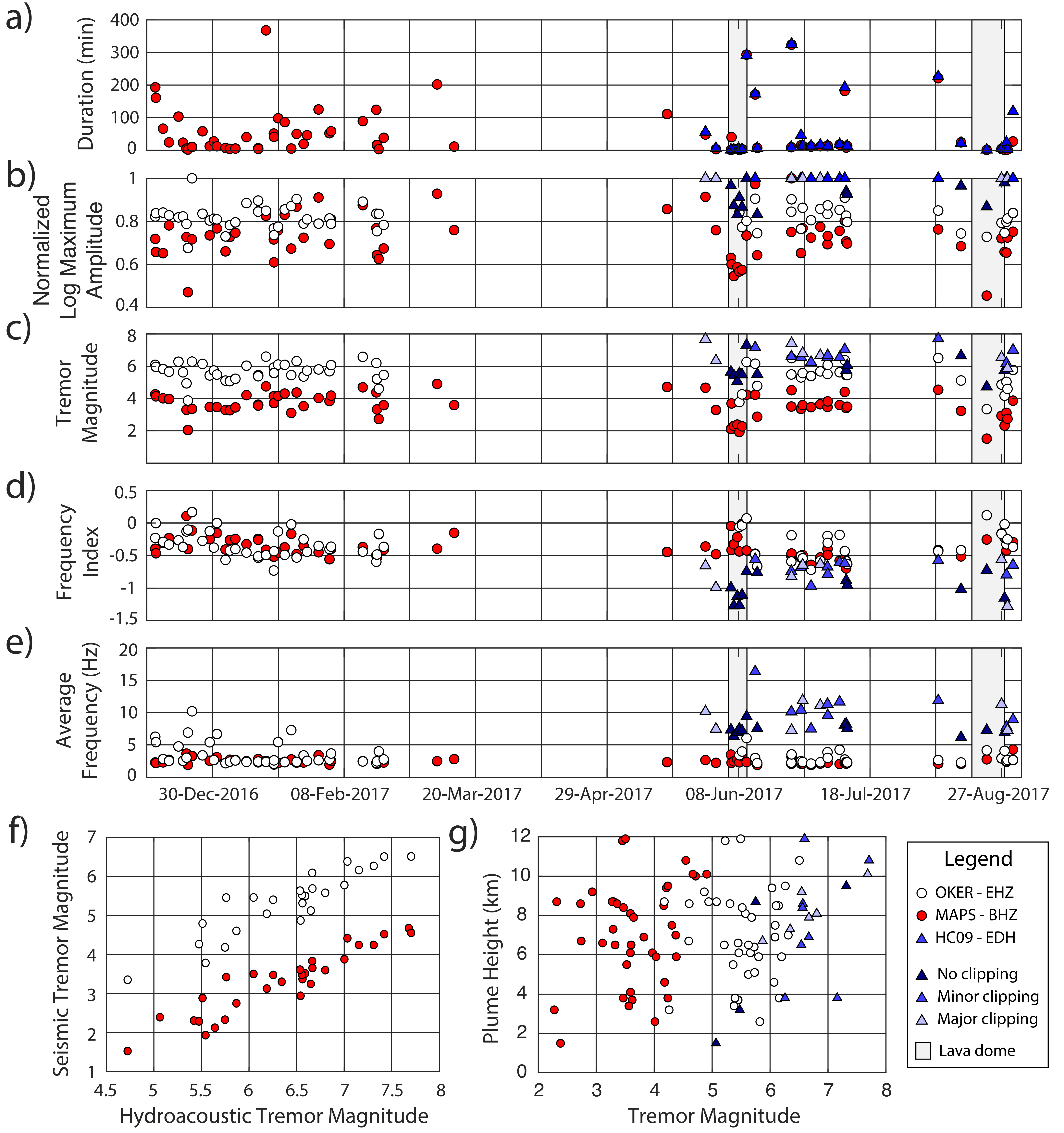

a)
Duration (min)
b)
Normalized Log Maximum Amplitude
c)
Tremor Magnitude
d)
Frequency Index
e)
Average Frequency (Hz)
30-Dec-2016
08-Feb-2017
20-Mar-2017
29-Apr-2017
08-Jun-2017
18-Jul-2017
27-Aug-2017
f)
Seismic Tremor Magnitude
Hydroacoustic Tremor Magnitude
g)
Plume Height (km)
Tremor Magnitude
Legend
OKER - EHZ
MAPS - BHZ
HC09 - EDH
No clipping
Minor clipping
Major clipping
Lava dome

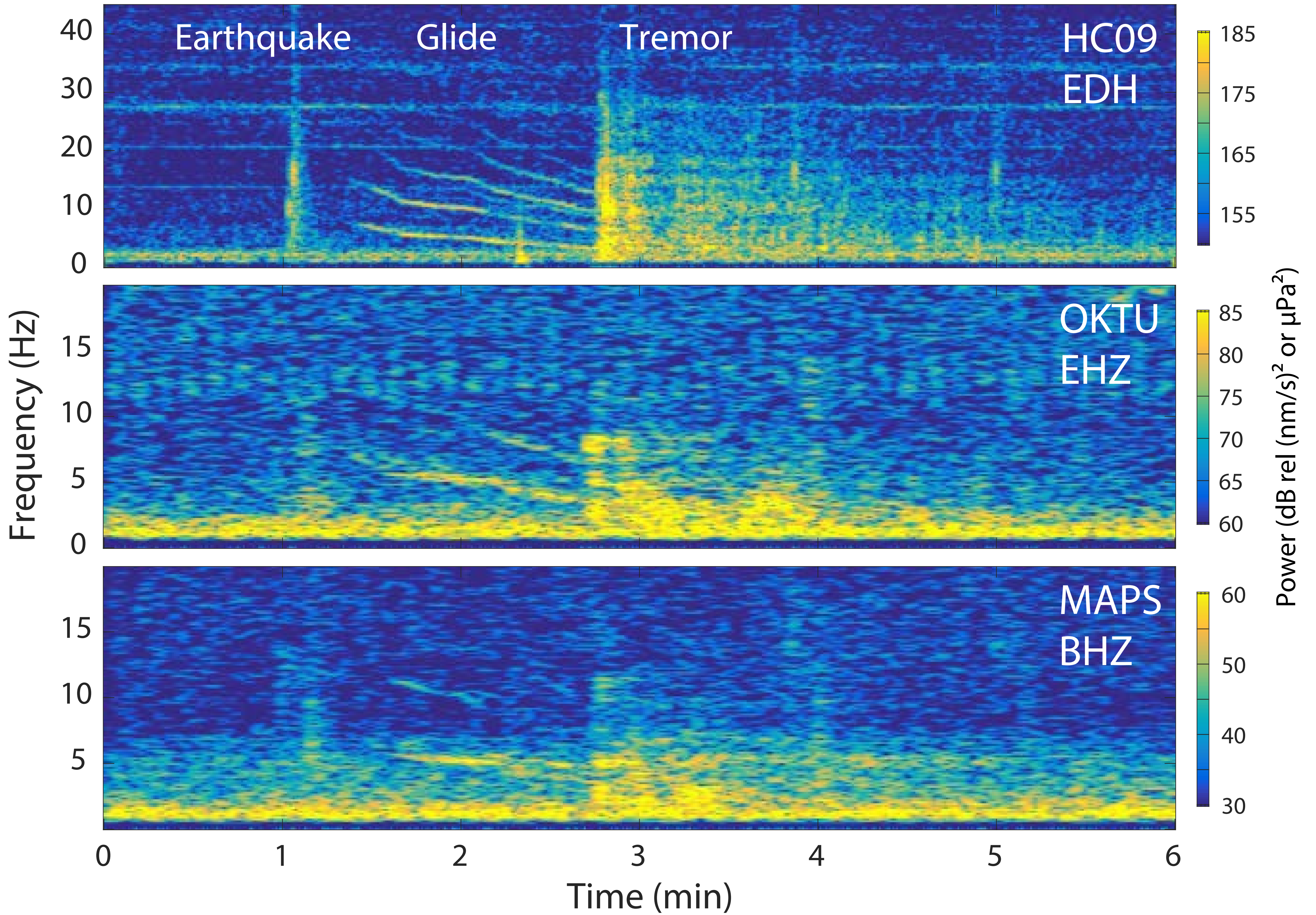

Earthquake
Glide
Tremor
HC09
EDH
OKTU
EHZ
MAPS
BHZ
Frequency (Hz)
Time (min)
Power (dB rel (nm/s)² or μPa²)
0 10 20 30 40
0 5 10 15
5 10 15
0 1 2 3 4 5 6
155 165 175 185
60 65 70 75 80 85
30 40 50 60

a)
Starting at 2017-06-24 00:45
b)
Starting at 2017-06-27 11:15
c)
Starting at 2017-07-05 03:02
d)
Starting at 2017-08-27 00:27
HC09
MAPS
Frequency (Hz)
Time (min)
Power (dB re (nm/s)^2 or uPa^2)

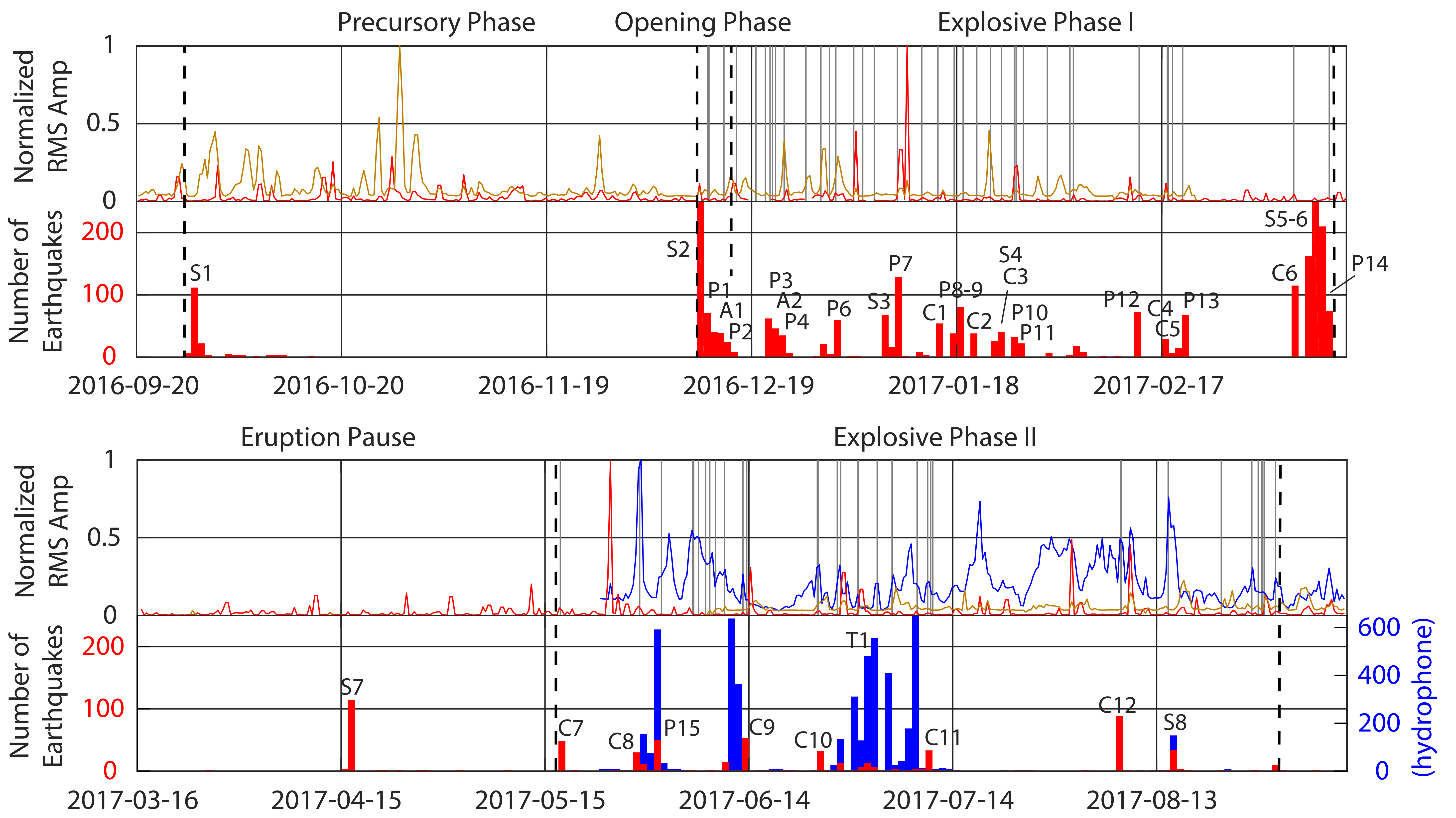
Precursory Phase
Opening Phase
Explosive Phase I
Normalized RMS Amp
Number of Earthquakes
1
0.5
0
200
100
0
S1
S2
P1
A1
P2
P3
A2
P4
P6
S3
P7
C1
P8-9
C2
S4
C3
P10
P11
P12
C4
C5
P13
C6
S5-6
P14
2016-09-20
2016-10-20
2016-11-19
2016-12-19
2017-01-18
2017-02-17
Eruption Pause
Explosive Phase II
S7
C7
C8
P15
C9
C10
T1
C11
C12
S8
600
400
200
(hydrophone)
2017-03-16
2017-04-15
2017-05-15
2017-06-14
2017-07-14
2017-08-13

Volcano	Location	Eruption Dates	Nearest Seismic Station (km)	Nearest Hydrophone (km)	Nearest Acoustic Sensor (km)	Reference
Capelinhos	Azores	Sep 1957 - Oct 1958	20	local	local	Richards, 1963
Surtsey	Iceland	Nov 1963 - Jun 1967	22	N/A	N/A	Pálmason, 1966; Sigtryggson & Sigurðsson, 1966
Myojin-sho	Japan	Sep 1952 - Oct 1953	N/A	8600	N/A	Dietz and Sheehy, 1954
		Jan - Jul 1970	N/A	3000	N/A	Johnson and Norris, 1972
Nishinoshima	Japan	Feb - Nov 2015	1.5 (ocean-bottom seismometer)	N/A	local	Shinohara et al., 2017
Hunga Tonga - Hunga Ha'apai	Tonga	Mar 2009	global	160	N/A	Bohnenstiehl et al., 2013
		Dec 2014 - Jan 2015	N/A	9000	1845	Smink, 2017
Bogoslof	Alaska	Sep 2016 - Aug 2017	50	7	60	This study
Sholan	Red Sea	Apr - Dec 2011	regional	N/A	N/A	Xu et al., 2015
Jadid	Red Sea	Dec 2012 - Sep 2013	regional	N/A	N/A	Xu et al., 2015

Station	Sensor Type	Network	Percent Data Return*	Major outage start time	Major outage end time
OKER	Short-period	Okmok	65.9	21 Feb 2017, 19:27	8 Jun 2017, 00:36
OKRE	Short-period	Okmok	48.5	21 Feb 2017, 19:27	8 Jun 2017, 00:36
OKTU	Short-period	Okmok	63.6	21 Feb 2017, 19:27	8 Jun 2017, 00:36
OKFG	Broad-band	Okmok	89.7	18 Dec 2016, 07:04	21 Dec 2016, 21:08
MAPS	Broad-band	Makushin	95.0	18 Dec 2016, 07:19	21 Dec 2016, 20:20
MGOD	Broad-band	Makushin	94.4	18 Dec 2016, 07:19	21 Dec 2016, 20:24
MREP	Short-period	Makushin	68.1	21 Feb 2017, 19:27	8 Jun 2017, 00:36
MSW	Short-period	Makushin	N/A	7 Sep 2016, 11:38	12 Sep 2016, 20:32

Number*	Analyst Start	Analyst End	MAPS Start	MAPS End	# of events (MAPS)	Average rate (#/hr)	Max rate (#/hr)	Associated Explosion #**	Merged into tremor?
S1	9/28/2016 5:55	9/28/2016 23:52	9/28/2016 5:46	9/29/2016 1:21	114	5.82	20	-	-
S2	12/11/2016 0:30	12/12/2016 1:45	12/11/2016 5:20	12/12/2016 0:00	288	15.43	40	-	-
P1	12/12/2016 4:15	12/12/2016 13:05	12/12/2016 4:15	12/12/2016 15:10	40	4.55	20	1?	Y
A1	12/12/2016 21:27	12/13/2016 9:18	12/12/2016 22:07	12/13/2016 5:52	31	4	32	2	Y
P2	12/14/2016 20:40	12/14/2016 21:55	12/14/2016 20:57	12/14/2016 21:50	36	40.75	48	3	Y
P3	12/21/2016 10:36	12/21/2016 16:00	station outage	-	-	-	-	un	Y
A2	12/21/2016 17:15	12/21/2016 18:25	station outage	-	-	-	-	un	Y-short
P4	12/21/2016 19:54	12/22/2016 1:05	12/21/2016 20:37	12/22/2016 0:59	80	18.32	44	7	Y
P5	12/30/2016 2:40	12/30/2016 8:30	partial station outage	-	-	-	-	12	Y
P6	12/30/2016 21:45	12/31/2016 7:27	12/31/2016 3:44	12/31/2016 7:21	43	11.89	32	13	Y
S3a	1/7/2017 5:55	1/7/2017 16:30	1/7/2017 6:57	1/7/2017 9:09	11	5	12	-	-
S3b	-	-	1/7/2017 10:20	1/7/2017 16:28	44	7.17	24	-	-
P7	1/8/2017 19:02	1/9/2017 7:24	1/8/2017 19:01	1/9/2017 7:24	133	10.74	104	17	Y
P8	1/17/2017 11:43	1/17/2017 14:27	1/17/2017 12:21	1/17/2017 15:00	25	12.1	32	21	Y-ish
P9	1/18/2017 11:27	1/18/2017 22:18	1/18/2017 10:56	1/18/2017 22:18	65	5.72	40	23	Y
S4	1/23/2017 5:50	1/23/2017 7:25	1/23/2017 5:51	1/23/2017 7:23	22	14.35	32	-	-
P10	1/26/2017 10:24	1/26/2017 10:36	1/26/2017 10:24	1/26/2017 10:38	25	107.14	100	un	Y
P11	1/27/2017 16:47	1/27/2017 17:17	1/27/2017 16:47	1/27/2017 17:10	22	57.39	60	28	Y
P12	2/13/2017 15:36	2/13/2017 16:13	2/13/2017 13:38	2/13/2017 20:07	21	8.24	24	32	-
P13	2/19/2017 20:42	2/20/2017 2:08	2/19/2017 20:41	2/20/2017 2:07	78	14.36	64	36	Y
S5	3/10/2017 2:50	3/10/2017 23:00	3/10/2017 2:53	3/10/2017 21:36	159	8.5	28	-	-
S6	3/11/2017 4:00	3/11/2017 15:25	3/11/2017 3:02	3/11/2017 14:12	276	24.72	80	-	-
P14	3/11/2017 18:16	3/13/2017 11:31	3/11/2017 18:45	3/13/2017 11:41	297	7.31	36	38	-
S7	4/15/2017 23:34	4/16/2017 2:15	4/15/2017 23:44	4/16/2017 2:36	114	39.77	96	-	-
P15	5/31/2017 16:00	5/31/2017 22:25	5/31/2017 19:26	5/31/2017 22:19	46	15.95	28	41	-
T1	7/1/2017 3:17	7/1/2017 5:35	7/1/2017 3:17	7/1/2017 5:35	12	5.22	12	-	-
S8	8/15/2017 8:10	8/15/2017 16:05	8/15/2017 8:52	8/15/2017 13:56	21	4.14	16	-	-

Number*	Analyst Start	Analyst End	HC09 Start	HC09 End	# of events	Average rate (#/hr)	Max rate (#/hr)	Associated Explosion #**	Merged into tremor?
HA1	29-May-17 1:14	29-May-17 13:24	29-May-17 2:55	29-May-17 11:36	59	6.79	24	40	-
HS1	29-May-17 15:17	30-May-17 9:18	29-May-17 15:19	30-May-17 11:12	131	6.59	64	-	-
HS2	30-May-17 16:24	30-May-17 23:34	30-May-17 15:19	31-May-17 0:05	40	4.56	16	-	-
HP1	31-May-17 14:50	31-May-17 22:25	31-May-17 15:06	1-Jun-17 1:32	585	56.07	168	41	-
HA2	1-Jun-17 10:06	1-Jun-17 13:52	1-Jun-17 10:06	1-Jun-17 13:53	21	5.55	16	41	-
HP2	8-Jun-17 23:06	9-Jun-17 0:55	-	-	-	-	-	47	Y
HP3	11-Jun-17 10:39	13-Jun-17 1:26	11-Jun-17 12:11	13-Jun-17 0:13	994	27.59	104	49	-
HA3	13-Jun-17 4:41	13-Jun-17 9:56	13-Jun-17 4:41	13-Jun-17 8:48	21	5.1	20	49	-
HP4	23-Jun-17 21:26	23-Jun-17 23:14	-	-	-	-	-	51	-
HP5	26-Jun-17 23:42	27-Jun-17 0:39	26-Jun-17 21:49	27-Jun-17 0:39	131	46.24	284	53	-
HS3	29-Jun-17 5:36	29-Jun-17 6:03	29-Jun-17 5:31	29-Jun-17 5:54	43	112.17	144	-	-
HP6	29-Jun-17 14:23	30-Jun-17 1:03	29-Jun-17 10:41	30-Jun-17 1:02	271	18.89	64	55	-
HP7a	30-Jun-17 16:37	2-Jul-17 19:37	30-Jun-17 17:01	2-Jul-17 18:44	1151	23.15	88	56	-
HP7b (RRE)	2-Jul-17 19:37	2-Jul-17 20:47	-	-	-	-	-	56	Y
HP8	4-Jul-17 4:14	4-Jul-17 21:09	4-Jul-17 2:46	4-Jul-17 21:08	408	22.21	56	57	-
HP9	6-Jul-17 12:16	8-Jul-17 17:43	6-Jul-17 13:09	8-Jul-17 17:44	862	16.39	220	59	-
HA4	7-Aug-17 21:16	7-Aug-17 23:39	-	-	-	-	-	63	-
HS4	15-Aug-17 4:15	17-Aug-17 15:01	15-Aug-17 4:28	15-Aug-17 6:33	149	71.52	120	-	-

Number	MAPS Start	MAPS End	# of events (MAPS)	Average rate	Max rate	Co-eruptive Explosion #
C1	1/15/2017 6:51	1/15/2017 12:00	44	8.54	68	20
C2	1/20/2017 22:17	1/20/2017 22:55	21	33.16	40	24
C3	1/24/2017 13:54	1/24/2017 14:35	22	32.2	56	26
C4	2/13/2017 16:31	2/13/2017 17:52	45	33.33	52	32
C5	2/17/2017 19:03	2/17/2017 21:09	27	12.86	28	33
C6	3/8/2017 7:20	3/8/2017 10:58	107	29.45	92	37
C7	5/17/2017 6:32	5/17/2017 8:04	39	25.43	44	39
C8	5/28/2017 22:18	5/28/2017 23:02	29	39.55	48	40
C9	6/13/2017 1:53	6/13/2017 4:35	27	10	32	49
C10	6/24/2017 3:18	6/24/2017 8:42	20	3.7	20	52
C11	7/10/2017 7:48	7/10/2017 10:33	22	8	24	60
C12	8/7/2017 16:54	8/7/2017 21:16	75	17.18	60	63